Materials Today Bio 32 (2025) 101737

Contents lists available at ScienceDirect

Materials Today Bio

journal homepage: www.journals.elsevier.com/materials-today-bio

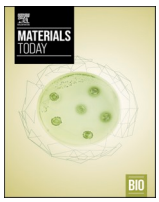

Bi-phasic integrated silk fibroin/polycaprolactone scaffolds for osteochondral regeneration inspired by the native joint tissue and interface

Zexing Zhang [a], Qingquan Dong [a], Zubing Li [a], Gu Cheng [b,*], Zhi Li [a,**]

[a] State Key Laboratory of Oral & Maxillofacial Reconstruction and Regeneration, Key Laboratory of Oral Biomedicine Ministry of Education, Hubei Key Laboratory of Stomatology, School & Hospital of Stomatology, Wuhan University, Wuhan, 430072, China
[b] Department of Oral and Maxillofacial Surgery, School and Hospital of Stomatology, Wenzhou Medical University, Wenzhou, 325027, China

ARTICLE INFO

Keywords:
Integrated scaffold
Osteochondral defect
Tissue engineering
Gas foaming
Wet electrospinning

ABSTRACT

Osteochondral scaffolds designed with bi-phasic and multi-phasic have typically struggled with post-implantation delamination. To address this issue, we developed a novel integrated scaffold with natural and continuous interface and heterogeneous bilayer structure. Through layer-by-layer wet electrospinning, two-dimensional (2D) bi-layer integrated membranes of silk fibroin (SF) and polycaprolactone (PCL) were fabricated. These membranes were then transformed into three-dimensional (3D) scaffolds using a CO_2 gas foaming technique, followed by gelatin coating on the osteogenic layer to afford final bi-phasic porous scaffolds. *In vitro* studies indicated that the 3D scaffolds better-maintained cell phenotypes than conventional 2D electrospun films. Additionally, the 3D scaffolds showed superior cartilage repair and osteoinductivity potential, with increased subchondral bone volume and reduced defect area in rat osteochondral defects models at 12 weeks. Taken together, these gas-foamed scaffolds were a promising candidate for osteochondral regeneration.

1. Introduction

Osteoarthritis (OA) is a prevalent joint disease affecting approximately 14.8 % of people over the age of 30 years globally [1]. As a chronic progressive disease, OA is characterized by joint pain, functional impairment, and osteochondral defects resulting from the degradation of the cartilage extracellular matrix and the destruction of subchondral bone [2,3]. Mature cartilage has a limited self-repair capacity due to the absence of blood vessels and nerves, necessitating clinical intervention following injury [4,5]. Traditional treatments, such as microfracture, autologous osteochondral grafting, and artificial joint implantation, face high failure rates and limited regenerative outcomes [6–9]. With the development of tissue engineering, artificial osteochondral scaffolds that integrate cell biology with materials science, have emerged as a promising alternative to conventional surgical approaches.

In recent years, various monophasic, bi-phasic and multi-phasic scaffolds have been designed to repair osteochondral defects [10–13]. Monophasic scaffolds inherently lack the requisite physical architecture necessary to guide osteochondral tissue regeneration, often resulting in uniformly regenerated tissue throughout the scaffold [13]. The bi-phasic and multi-phasic scaffolds more closely mimic the native osteochondral tissue architecture, enabling improved repair outcomes [14]. These methods are relatively straightforward, allowing for tailored material selection and fabrication techniques to meet the specific compositional and morphological requirements of cartilage and subchondral bone. Despite these advantages, achieving a natural interface with anisotropic and heterogeneous properties within osteochondral scaffolds remains challenging [7,15,16]. Most current designs construct individual layers separately, later bonding them into a single entity using techniques such as adhesive bonding and freeze-drying [17–19]. The discontinuous and abrupt interfaces created are prone to delamination, thus compromising the repair efficacy of osteochondral tissue [20–22]. This study aimed to address these challenges by constructing integrated osteochondral scaffolds with smooth and biomimetic junctions using a novel combination of wet-electrospinning and gas foaming technologies.

Wet-electrospinning, a recent technological advancement, integrated electrospinning and wet spinning. Instead of utilizing a solid collector, this method employed liquid bathes to collect the electrospun fibers [23]. During the electrospinning process, liquid adhered to the surface of the nanofibers, preventing direct contact between fibers and inhibiting their adhesion, which can form a loose structure of scaffolds [24,25]. However, the thickness increase of nanofibrous scaffolds

* Corresponding author.
** Corresponding author.
E-mail addresses: gucheng@whu.edu.cn (G. Cheng), zhili@whu.edu.cn (Z. Li).

https://doi.org/10.1016/j.mtbio.2025.101737
Received 12 November 2024; Received in revised form 5 February 2025; Accepted 5 April 2025
Available online 8 April 2025

produced by wet-electrospinning was limited, and difficult to meet the required specifications for osteochondral regeneration scaffolds [26].

Gas foaming technology offered a solution by generating bubbles to stretch 2D electrospun films into 3D scaffolds. This technique preserved the original topological alignment of the fibers and guided cellular migration along them [27]. Previous studies have demonstrated the ability of gas foaming to modify scaffold architecture, with Chen et al. using sodium borohydride ($NaBH_4$) to expand 2D membranes into 3D structure scaffolds, which has been demonstrated to promote neocartilage regeneration *in vivo* [28]. More recently, Xie et al. employed modified gas foaming technology to expand 2D membranes to construct various 3D structure scaffolds, and have demonstrated the potential for application in multiple tissue repair applications (osteogenic, angiogenesis, wound dressing) [29,30]. However, to our knowledge, the combination of wet electrospinning and gas foaming to transform 2D membranes into 3D heterogeneous scaffolds for osteochondral repair has not been fully explored.

In this study, we first fabricated bi-layer two-dimensional (2D) electrospun membranes in one-step by layer-by-layer wet-electrospinning process. Then, gas foaming technology was employed to convert these 2D membranes into three-dimensional (3D) scaffolds (Fig. 1). This transformation could enhance cellular infiltration and more effectively mimic the osteochondral microenvironment than 2D membranes [31]. Finally, a gelatin coating was applied *in situ* to the osteogenic layer to enhance its mechanical properties, while the chondrogenic layer maintains a flexible compressive strength and a hypoxic environment conducive to chondrogenic differentiation [32]. This study aims to contribute to the development of biomimetic scaffolds designed for osteochondral tissue and interface regeneration.

2. Materials and methods

2.1. Materials

Silk cocoons were purchased from Shenzhou Union Silk Co. Ltd. (Zhejiang, China). Gelatin, polycaprolactone (PCL, Mn = 80 kDa), ethanol, and 1,1,1,3,3,3-hexafluoro-2-propane (HFIP) were sourced from Sigma-Aldrich (MO, USA). Dulbecco's Modified Eagle's Medium (DMEM), α-modified Eagle's medium (α-MEM), 1 % insulin-transferrin-sodium selenite (ITS), fetal bovine serum (FBS) and penicillin/streptomycin were sourced from HyClone (Beijing, China). Osteogenic culture medium was obtained from Cyagen (MUXMT-90021, Guangzhou, China). The calcein-AM/PI Double Stain, CCK-8 assay kit, and Actin-Tracker Green 488 were procured from Yeasen Biotechnology (Shanghai, China). DAPI, 1,1′-dioctadecyl-3,3,3′,3′-tetramethylindocarbocyanine perchlorate (Dil), and 3,3′-dioctadecyloxacarbocyanine perchlorate (DIO) were acquired from Beyotime Biotechnology (Shanghai, China). All reagents and supplies used were of analytical grade, without further processing.

2.2. Synthesis of the 3D osteochondral scaffolds

The 3D osteochondral scaffolds were synthesized via layer-by-layer wet-electrospinning, CO_2 gas foaming, and gelatin-coating for the osteogenic layer. SF and PCL (1:3 and 1:4, w/w) were dissolved into HFIP at a total concentration of 15 % (w/v), respectively. The electrospinning parameters were set as follows: a 75 % ethanol solution was utilized as the collector, the needle-to-collector distance was maintained at 16 cm, the voltage was fixed at 16 kV, and the flow rate was set at 0.5 ml/h. The $SP_{(1:3)}$ layer was obtained through 4 h of wet-electrospinning, immediately followed by an additional 4 h to attach the $SP_{(1:4)}$ layer onto the $SP_{(1:3)}$ layer. This electrospinning way formed an ethanol/water layer on the fiber surface, effectively preventing adhesion and direct contact between the fibers. Then the space between the fibers was filled with CO_2-saturated ethanol by immersing the bilayer membranes in a saturated ethanol/dry ice bath for 15 min, followed by immediate transfer to distilled water for 30 min. During this process, CO_2 gas rapidly escaped from the electrospun membranes due to its lower solubility in water compared to anhydrous ethanol, Then the membranes were rapidly swelled and transformed into 3D scaffolds with a larger

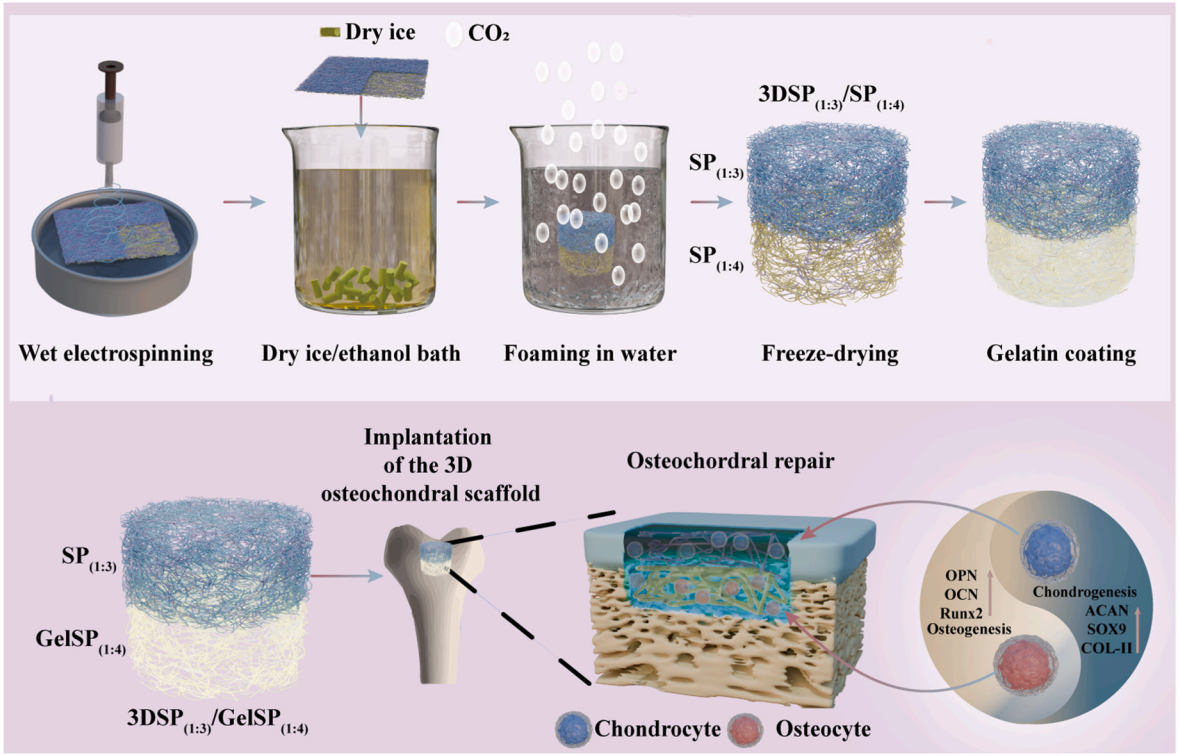

Fig. 1. Schematic illustration for the construction and functionalization of $3DSP_{(1:3)}/GelSP_{(1:4)}$.

volume, achieved by the enlargement of pore size. Subsequently, the scaffolds were placed in liquid nitrogen for 20 min and freeze-dried to maintain their 3D shape and structure. Finally, 10 % gelatin was spin-coated to the $SP_{(1:4)}$ layer [33,34], yielding $3DSP_{(1:3)}/GelSP_{(1:4)}$ scaffolds. For comparison, a $2DSF/PCL_{(1:3)}$/gelatin coated $SF/PCL_{(1:4)}$ membranes, denoted as $2DSP_{(1:3)}/GelSP_{(1:4)}$ were prepared using the identical electrospinning parameters.

2.3. Characteristics of the 2D/3D scaffolds

To investigate the impact of gas foaming on scaffold characteristics, the 2D/3D $SP_{(1:3)}/SP_{(1:4)}$ scaffolds were analyzed by Fourier transform infrared spectroscopy (FTIR, Nicolet 170-SX, Thermo Nicolet Ltd., USA), X-ray photoelectron spectroscopy (XPS, Kratos, UK), X-ray diffractometry (XRD, XPert Pro, Holland).

The surface and cross-sectional morphologies of the 2D/3D $SP_{(1:3)}/SP_{(1:4)}$, 2D/3D $SP_{(1:3)}/GelSP_{(1:4)}$ scaffolds were analyzed by scanning electron microscopy (SEM, FE-SEM, ZEISSΣ SIGMA, Germany). The pore size distribution of at least 50 pores in each scaffold was measured and quantified by ImageJ software based on the SEM images. Porosity(P) was calculated using a theory from a previous study [5]:

$$P(\%) = 1 + \frac{1 - (D1/D2)^3}{\left(1 + \left[W_1/W_2\right]X\rho\right)}$$

where ρ represents the density of ethanol at 24 °C, saturated weight (W_1) and diameter (D_1), dry scaffold weight (W_2) and diameter (D_2). The swelling ratio was calculated using the following formula:

$$\text{Swelling ratio } (\%) = \frac{(w1 - wd)}{wd}$$

where W_d is the weight of the dried scaffold, W_1 is the weight of the scaffold soaked in PBS at 37 °C for 24 h, and the surface was then dried with filter paper before being weighed. The *in vitro* degradation assay was perform by immersing the $3DSP_{(1:3)}$, $3DGelSP_{(1:4)}$, and $3DSP_{(1:3)}/GelSP_{(1:4)}$ scaffolds (10mm × 10mm × 5 mm) into lipase solutions (0 U/mL and 2 U/mL, n = 4) and incubating at 37 °C under constant agitation (100 rpm). After 4 weeks of incubation, the scaffolds were washed, freeze-dried, and finally calculated their mass loss as follow:

$$\text{Degradation ratio } (\%) = \frac{(W_1 - W_2)}{W1}$$

where W_1 and W_2 denote the initial and remaining dry masses, respectively.

The compressive test was conducted using a universal-materials testing machine (CMT4053, JiNan MTS Test Technology Co., Ltd, China). Briefly, the 3D scaffolds (5 mm × 10 mm × 10 mm) were subjected to compression at a rate of 2 mm/min. Uniaxial compression was measured from 0 % to 60 % strain, while isostatic circulation was repeated 50 times between 0 % and 20 % strain to assess fatigue resistance. The tensile properties of the 3D scaffolds (5 mm × 10 mm × 30 mm) were assessed using the same testing machine, applying a tensile force at a constant rate of 5 mm/min.

Rheological tests were employed to evaluate the bonding strength between the osteogenic and chondrogenic layers of the 3D integrated scaffolds by replicating the shear stress environment of joint tissues and interfaces. Two control groups were employed for comparative analysis: One was fabricated by physically overlaying $SP_{(1:3)}$ layer onto the $GelSP_{(1:4)}$ layer without further processing steps ($3DSP_{(1:3)}$ + $GelSP_{(1:4)}$). The other one is constructed by overlaying $SP_{(1:3)}$ layer onto the $GelSP_{(1:4)}$ layer, followed by freeze-drying (F-$3DSP_{(1:3)}$ + $GelSP_{(1:4)}$). Frequency sweeps were conducted at deflection frequencies of 0.1–10 Hz, with a constant shear strain (1 %) and temperature (25 °C). Amplitude sweeps were conducted at a fixed frequency (10 Hz) and temperature (25 °C), with shear strain ranging from 1 % to 55 %.

2.4. Cell counting Kit-8 (CCK-8)

The Mouse Calvaria Osteoblastic Cell Line (MC3T3-E1) and ATDC5 cell lines were employed in this experiment. During the osteogenic differentiation, MC3T3-E1 cells gradually form mineralized bone-like matrix and exhibit osteoblast-specific functions such as the expression of bone related markers (such as alkaline phosphatase, osteocalcin) [35,36]. The pre-chondrogenic ATDC5 cell line, derived from mouse embryonic pancreatic cells, has become an ideal research model due to its ability to simulate the entire process from chondrogenic progenitors to mature chondrocytes [37,38].

The proliferation of MC3T3-E1 and ATDC5 cells, which were seeded on the osteogenic and chondrogenic layers of the 2D/3D $SP_{(1:3)}/GelSP_{(1:4)}$ scaffolds respectively, was assessed using the CCK-8 assay. Briefly, the scaffolds with the diameter of 6 mm were placed into 96-well plates, with $5x10^3$ cells seeded in each well. After 1, 3, and 7 days, the cell/scaffold complexes were further cultured with 10 μl CCK-8 solution and 90 μl fresh medium at 37 °C for 1 h. The absorbance value was measured at 450 nm using a microplate spectrophotometer (Biotek Instruments, USA).

2.5. Live/dead staining assay

The biocompatibility of the 2D membranes and 3D scaffolds was also assessed by a live/dead staining assay. MC3T3-E1 and ATDC5 cells were seeded on the osteogenic and chondrogenic layers of the 2D/3D $SP_{(1:3)}/GelSP_{(1:4)}$ scaffolds, respectively. After 3 days, the cell/scaffold complexes were treated with a live/dead staining working solution containing 1 mM calcein-AM and 2 mM propidium iodide, according to the manufacturer's protocol, for 30 min. The stained complexes were then washed 3 times with PBS and examined under a confocal laser scanning microscope (CLSM) (FV3000, Olympus, Japan).

2.6. Cytoskeleton staining assay

ATDC5 and MC3T3-E1 cells were cultured on the 2D/3D $SP_{(1:3)}/GelSP_{(1:4)}$ scaffolds for 3 days. Following fixation with 4 % paraformaldehyde and permeabilized using 0.1 % Triton-X. The cell/scaffold complexes were stained with Actin-Tracker Green 488 and counterstained with DAPI. Imaging was performed using CLSM.

2.7. Cell distribution in the 3D osteochondral scaffolds

To distinguish and observe cells distribution in different layers of the integrated $3DSP_{(1:3)}/GelSP_{(1:4)}$ scaffolds (10mm × 10mm × 5 mm), Dil (red)- and Dio (green)- labeled cells were prepared according to the protocol in the previous study [39]. To minimize interlayer cell mixing, a sequential seeding procedure with an optimized incubation period was employed. Specifically, 200 μL of Dio-labeled MC3T3-E1 cells ($2.5x10^6$ cells/cm^3) was seeded onto the $GelSP_{(1:4)}$ osteogenic layer of the $3DSP_{(1:3)}/GelSP_{(1:4)}$ scaffold and then incubated at 37 °C for 2 h, facilitating sufficient cells adhesion onto the scaffold and preventing the displacement of cells from the scaffold. Subsequently, the MC3T3-E1 cells-seeded scaffold was carefully inverted, seeded with 200 μL of DiI-labeled ATDC5 cells onto the other layer (Chondrogenic $SP_{(1:3)}$ layer) of the $3DSP_{(1:3)}/GelSP_{(1:4)}$ scaffold and incubated for another 2 h. After 7 days of *in vitro* culture, the cells/scaffold complexes were fixed with 4 % paraformaldehyde, then cut into halves from the axial position to the exposed section, which would be observed through CLSM.

2.8. Immunofluorescence staining

The osteogenic and chondrogenic potentials of the 2D/3D $SP_{(1:3)}/GelSP_{(1:4)}$ scaffolds were evaluated *in vitro* by immunofluorescence staining. Briefly, the osteogenic induced MC3T3-E1 cells were seeded onto the osteogenic $GelSP_{(1:4)}$ layer, and the chondrogenic induced

ATDC5 cells were seeded on the chondrogenic $SP_{(1:3)}$ layer. After 14 days of *in vitro* culture, cells/scaffold complexes were fixed in 4 % paraformaldehyde, permeabilized with 0.1 % Triton X-100 for 10 min, and blocked with 3 % BSA for 1 h. The cells were then incubated with the primary antibody against OCN (Proteintech, China, 1:500) and collagen II (Proteintech, China, 1:500) overnight respectively, followed by 1 h co-incubation with Cy3-conjugated fluorescence secondary antibody (Abclonal, China, 1:200). After counterstained with DAPI, the sections were observed using CLSM.

2.9. Real-time quantitative polymerase chain reaction (RT-qPCR)

The gene expression of chondrogenic and osteogenic genes, such as OCN, OPN, Runx2, Col-II, ACAN, and SOX9 in cells attached to various scaffolds were quantified using RT-qPCR. Briefly, total RNA was extracted utilizing an RNA extraction Kit (Omega, BIO-TEK, USA). The cDNA was synthesized using a Reverse Transcription Kit (Takara, Japan). The qPCR was performed on the CFX96 Connect RealTime PCR Detection System (BIO-RAD, USA) as follows: 95 °C for 15 s followed by 40 cycles (95 °C for 15 s and 60 °C for 30 s). Calculation of the relative expression level of the target gene was conducted using GAPDH as a housekeeping gene, applying the $2^{\Delta\Delta Ct}$ method. The relevant primer sequences are provided in Table S1.

2.10. Animal experiments

All procedures in the experiment were approved by the Institutional Animal Care and Use Committee of Wuhan University (S0792403029). Thirty male Sprague-Dawley (SD) rats (~200g) were randomly divided into three groups (control, $2DSP_{(1:3)}/GelSP_{(1:4)}$ and $3DSP_{(1:3)}/GelSP_{(1:4)}$). Briefly, after intraperitoneal anesthesia and disinfection, the femoral head was exposed, and defects with a depth and diameter of 2 mm were created on the femoral head using a trephine and filled with the $2DSP_{(1:3)}/GelSP_{(1:4)}$ and the $3DSP_{(1:3)}/GelSP_{(1:4)}$ respectively. The control group underwent the same surgical procedure as the other groups, but the defects were not filled. After 6 and 12 weeks of transplantation, the rats were euthanized through high-flow CO_2 and femurs were harvested, photographed, and assessed for cartilage defect repair utilizing the International Cartilage Repair Society (ICRS) grading system by two independent observers [40]. Micro-CT scans (Skyscan1276, Bruker) and histological analysis (Hematoxylin and Eosin (HE), Safranin O/Fast Green, and Masson's trichrome staining) were also conducted to evaluate the cartilaginous and subchondral tissue regeneration in the osteochondral defects. For the COL-II and OCN immunohistochemical staining, slices were incubated with 3 % hydrogen peroxide solution in the dark for 25 min, followed by blocking with 1.5 % rabbit serum for 20 min. Subsequently, the slices were incubated overnight at 4 °C with primary antibodies targeting Col-II and OCN (Proteintech, China), then incubated with horseradish peroxidase-conjugated secondary antibodies (Maxim Biotechnology, China) at room temperature for 30 min. The nuclei were then counterstained with hematoxylin and subsequently examined under a light microscope.

2.11. Statistical analysis

All data were analyzed using GraphPad prism 9 or Origin 2024 and are presented as mean ± standard deviation. Statistical significance was determined by an independent sample *t*-test and one-way analysis of variance (ANOVA). A p-value less than 0.05 was deemed to be statistically significant.

3. Results

3.1. Characterization of the 2D/3D scaffolds

As shown in Fig. S1, monophasic 3D scaffolds with varying SF/PCL ratios (1:2, 1:3, 1:4, 1:5) were fabricated to optimize the parameters for the final bi-phasic scaffolds. The mean pore diameters of the 1:2, 1:3, 1:4 and 1:5 monophasic scaffolds were 12.1 ± 5.5, 30.6 ± 5.1, 91.6 ± 28.3 and 21.6 ± 4.85 μm, respectively. In addition, no significant difference in porosity was observed across 3D monophasic scaffolds with different ratios, all of which exceeded 80 % (Fig. S2a). These results demonstrated that both very low and very high concentrations of PCL resulted in only minor changes in pore diameter. Therefore, SF/PCL ratios of 1:3 and 1:4 were selected to fabricate the chondrogenic and osteogenic layers in subsequent experiments.

The bi-phasic integrated scaffolds were fabricated through layer-by-layer wet-eletrospining and gas foaming (Fig. 1). The gross observation of the 2D/3D $SP_{(1:3)}/GelSP_{(1:4)}$ were shown in Fig. S1. The expansion 3D scaffolds with a thickness of about 5 mm were obtained, while the 2D films were only about 0.1 mm. The SEM images of nanofiber structure was different for each scaffold. The surface and cross-section of the 2D scaffold displayed a dense stacking structure, while the surface pores of the 3D scaffold were more obvious and exhibited natural and continuous transitions between interfaces (Fig. 2–3). The porosity of 3D scaffolds was 84.7 ± 2.3 %, which is significantly higher than that of 2D electrospun membranes (66 % ± 2.7 %). In summary, these results demonstrate that the 2D films were successfully transformed to bi-layer structure integrated 3D scaffolds.

FTIR, XPS, and XRD were used to study the effects of gas foaming on the chemistry and structure of components. 2D/3D $SP_{(1:3)}/SP_{(1:4)}$ scaffolds exhibited similar FTIR spectra (Fig. 2c). The characteristic peaks of SF (1650 cm^{-1} (amide I), 1538 cm^{-1} (amide II)) and PCL (2947 cm^{-1}(CH2 stretching), 1239 cm^{-1}(C-O-C stretching)) confirm the successful integration of SF and PCL in 2D/3D $SP_{(1:3)}/SP_{(1:4)}$ [41].

The XPS results (Fig. 2d) indicate that the atomic ratio of nitrogen (N) was too low to be detected in PCL, however, characteristic peaks of SF (N and Ca) were observed in both $3DSP_{(1:3)}/SP_{(1:4)}$ and $2DSP_{(1:3)}/SP_{(1:4)}$ samples. These results demonstrated that SF and PCL were successfully incorporated into the 2D/3D $SP_{(1:3)}/SP_{(1:4)}$ scaffolds.

In the XRD pattern (Fig. 2e), PCL diffraction peaks at 21.3° and 23.7° for the (110) and (200) planes, respectively, while the prominent SF peak at 22.5° overlapped with the strong PCL peak at 21.3° [42]. Nevertheless, the diffraction peaks of the 2D films are more pronounced than those of the 3D scaffolds. This suggests that the oriented crystalline structure of PCL was disrupted during the gas foaming process [43,44].

As shown in Fig. 3d, the surfaces of the $GelSP_{(1:4)}$ osteogenic layer of the $3DSP_{(1:3)}/GelSP_{(1:4)}$ scaffolds displayed a non-uniform gelatin distribution on the fiber surface after gelatin coating, without compromising the intrinsic transition between the chondrogenic and osteogenic layers. While no significant difference was observed in the average pore size, porosity, and swelling rate between the $GelSP_{(1:4)}$ layer and its uncoated state (Fig. 3 and S2), the gelatin modification significantly enhanced mechanical robustness, as evidenced by the higher maximum compression stress (50 cycles) and compressive modulus. Furthermore, the maximum compression stress and average compressive modulus were higher in the $GelSP_{(1:4)}$ layer than the $SP_{(1:3)}$ layer. In addition, the Young's modulus of the $GelSP_{(1:4)}$ layer (0.40 ± 0.06 MPa) was notably higher than that of the $SP_{(1:3)}$ layer (0.19 ± 0.02 MPa, Fig. 3h). This mechanical gradient closely mimics the native osteochondral tissue, where cartilage tissue exhibits a lower stiffness compared to that of the subchondral bone tissue [10,45].

Degradation behavior is one of the most critical factors influencing the post-implantation regenerative efficacy of osteochondral scaffolds [45,46]. As depicted in Fig. 3l, the degradation rate of all scaffolds was significantly accelerated at a concentration of 2 U/mL when compared with that of the 0 U/mL. Moreover, the degradation rate of the $3DSP_{(1:3)}$ layer was slightly higher than that of the $3DGelSP_{(1:4)}$ layer (Fig. 3h). Collectively, the $3DGelSP_{(1:4)}$ osteogenic layer of the $3DSP_{(1:3)}/GelSP_{(1:4)}$ scaffolds exhibited a longer degradation time than that $3DSP_{(1:3)}$ chondrogenic layer, which facilitated the subsequent process of bone regeneration with a longer time than that of cartilage

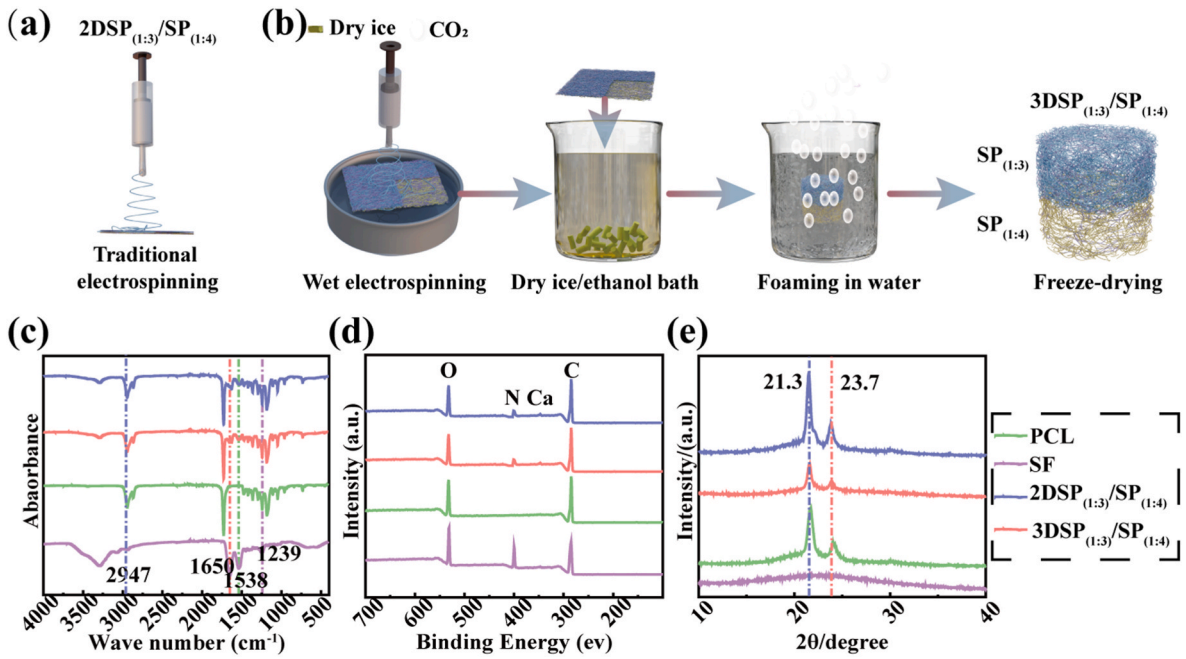

Fig. 2. Preparation and characterization of 2D/3D $SP_{(1:3)}/SP_{(1:4)}$. (a) Schematic illustration of preparation process of $2DSP_{(1:3)}/SP_{(1:4)}$. (b) Schematic illustration of preparation process of $3DSP_{(1:3)}/SP_{(1:4)}$. FTIR(c), XPS(d), XRD(e) spectra of the PCL, SF, $2DSP_{(1:3)}/SP_{(1:4)}$ and $3DSP_{(1:3)}/SP_{(1:4)}$.

repairing [12].

Rheological analysis were employed to assess the interfacial bonding strength between the osteogenic ($GelSP_{(1:4)}$) and chondrogenic ($SP_{(1:3)}$) layers of the $3DSP_{(1:3)}/GelSP_{(1:4)}$, F-$3DSP_{(1:3)}$ + $GelSP_{(1:4)}$ and $3DSP_{(1:3)}$ + $GelSP_{(1:4)}$ scaffolds (Fig. S2f-i). It is evident that the $3DSP_{(1:3)}/GelSP_{(1:4)}$ exhibited the highest storage modulus (G') among all groups. That means that an enhanced interfacial bonding strength could be observed at the interface of osteogenic and chondrogenic layers in the $3DSP_{(1:3)}/GelSP_{(1:4)}$ scaffold. Furthermore, under varying shear strain, the $3DSP_{(1:3)}/GelSP_{(1:4)}$ scaffold achieved the highest interfacial shear strength (2.61 ± 0.78 KPa) and torsional resistance (0.26 ± 0.08 mN m), followed by F-$3DSP_{(1:3)}$ + $GelSP_{(1:4)}$ and $3DSP_{(1:3)}$ + $GelSP_{(1:4)}$. These findings demonstrated that the $3DSP_{(1:3)}/GelSP_{(1:4)}$ scaffold possesses robust interfacial bonding strength and maintains structural stability under biomechanical shear stress.

3.2. Biocompatibility of the 2D/3D scaffolds

The cell proliferation of different scaffolds was evaluated by CCK-8 assay. As depicted in Figs. 4b and 5b, the proliferation rate of cells cultured on the $3DSP_{(1:3)}/GelSP_{(1:4)}$ was significantly higher at day 7 compared to other groups. Live-dead staining images were consistent with these results. As shown in Figs. 4c and 5a, minimal dead cells with red color were observed in both the $3DSP_{(1:3)}/GelSP_{(1:4)}$ and $2DSP_{(1:3)}/GelSP_{(1:4)}$ after 3 days of culture. Evaluation of cytoskeleton staining revealed that the both MC3T3-E1 and ATDC5 cells spread well on both scaffolds, with significant extension of pseudopodia (Figs. 4d and 5c). In addition, the well-designed 3D scaffolds supported cells in a characteristic spindle shape, whereas some cells on the 2D membranes adopted either a spherical morphology. The above results indicate that the porous structure provides space for cells to infiltrate and grow, which contributes to cell proliferation and spreading growth.

3.3. Osteogenic and chondrogenic differentiation in vitro

As shown in Fig. 4a, the $3DSP_{(1:3)}/GelSP_{(1:4)}$ scaffold exhibited a bi-layered structure. After 7 days of *in vitro* culture, majority of MC3T3-E1 cells and ATDC5 cells confined to their respective osteogenic and chondrogenic layers, with only limited cell mixing observed at the interface, which was consistent with the natural osteochondral interface, where a gradual transition between cartilage and subchondral bone occurs rather than a sharp boundary [45,47].

After 14 days of incubation, MC3T3-E1 cells in $3DGelSP_{(1:4)}$ layers exhibited higher level OCN expression levels than those on 2D scaffolds (Fig. 4h and S2l), consistent with the upward trends of osteogenic markers (OCN, OPN and RUNX2) observed via RT-qPCR (Fig. 4e–g). Particularly, the OCN expression of the $3DGelSP_{(1:4)}$ layers was 1.4 times higher than that in the 2D film group (Fig. 4g). Similarly, cells within $3DSP_{(1:3)}$ layers displayed more stronger COL-II immunofluorescence signals at 7 and 14 days compared to the2D controls (Fig. 5g and S2m). RT-qPCR findings were consistent with the COL-II immunofluorescence results, indicating that gene expression levels of SOX-9, ACAN, and COL-II in the 3D scaffolds were 2.7, 3.2 and 3.9 times higher than those in the 2D membranes, respectively (Fig. 5d–f). Collectively, these results indicate that the $3DSP_{(1:3)}/GelSP_{(1:4)}$ scaffolds demonstrated superior capacities in maintaining the phenotype of chondrocytes and osteoblasts than 2D membranes.

3.4. The repair efficacy of osteochondral defects in vivo

To further explore the potential therapeutic benefits of the 3D scaffolds *in vivo*, full-thickness osteochondral defects were established in rats (Fig. 6a). After 12 weeks of transplantation, large defects remained unfilled in the control groups and 2D films group. In contrast, defects in the $3DSP_{(1:3)}/GelSP_{(1:4)}$ group demonstrated a smaller and more regular appearance. Quantitative analysis using the ICRS scoring system (Fig. 6c) confirmed that the $3DSP_{(1:3)}/GelSP_{(1:4)}$ group obtained the highest macroscopic scores at both 6 (4.6 ± 0.4, $P < 0.05$) and 12 weeks (8.1 ± 0.3, $P < 0.05$) than those of the $2DSP_{(1:3)}/GelSP_{(1:4)}$ and control groups ($P < 0.05$).

To further investigate the efficacy of cartilage regeneration, samples were sliced and stained with Safranine O/Fast Green and Masson to assess proteoglycans distribution (Fig. 7c-d and S3). At 6 weeks post-operation, defect sites in the control group remained vacant and exhibited vascular hyperplasia, a classic symptom of inflammation (Fig. 7c). The defects in the $2DSP_{(1:3)}/GelSP_{(1:4)}$ groups were filled with

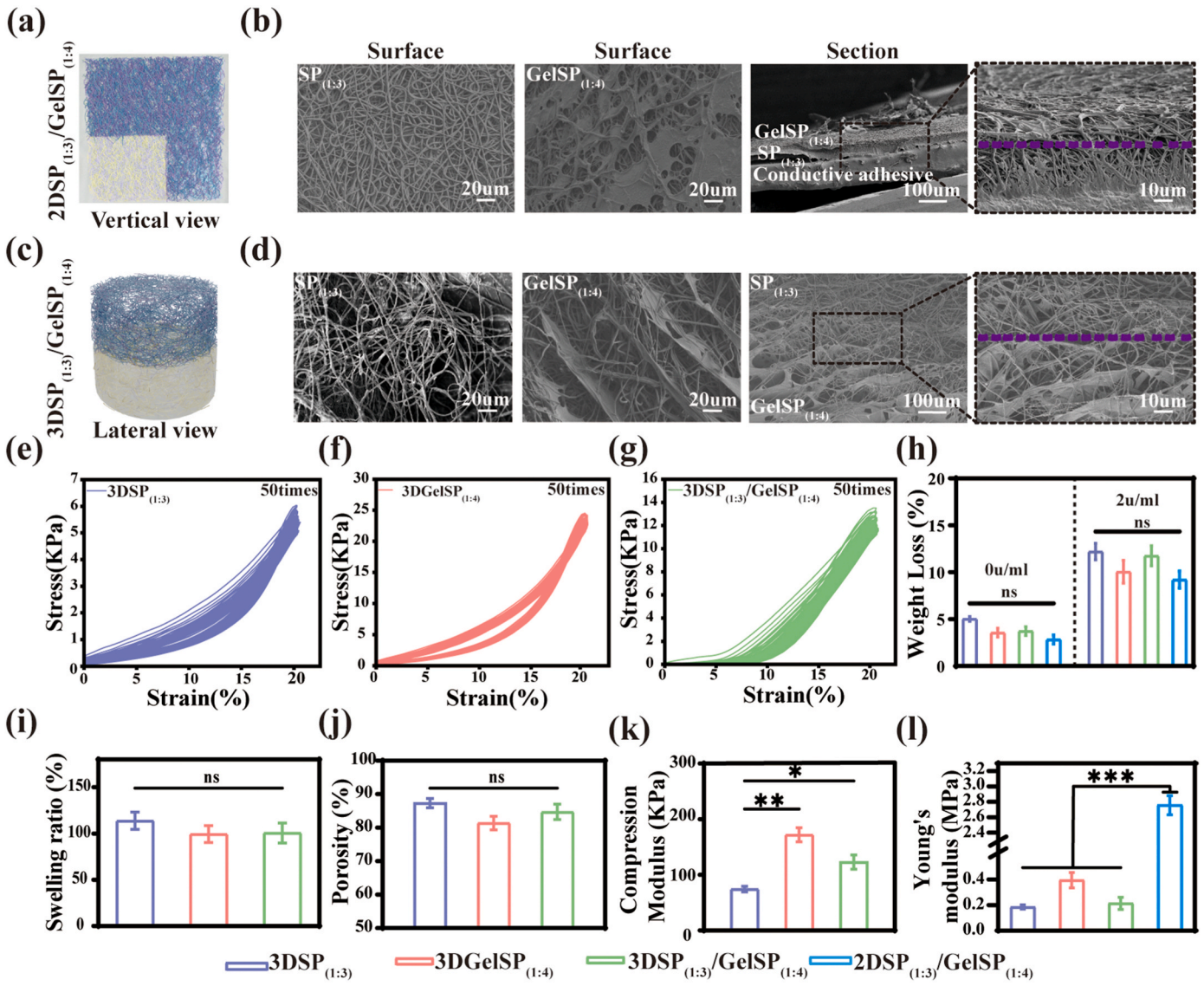

Fig. 3. Preparation and characterization of 2D/3D $SP_{(1:3)}$/$GelSP_{(1:4)}$. (a) Schematic diagrams depicting the vertical view of the preparation process for the gelatin coating on $2DSP_{(1:3)}$/$GelSP_{(1:4)}$. (b) SEM images of the surface and cross-section of $2DSP_{(1:3)}$/$GelSP_{(1:4)}$. (c) Schematic diagrams showcasing the lateral view of the preparation process for the gelatin coating on $3DSP_{(1:3)}$/$GelSP_{(1:4)}$. (d) SEM images of the surface and cross-section of $3DSP_{(1:3)}$/$GelSP_{(1:4)}$. (e–g) The cyclic compression stress–strain curves (50 times) of the $SP_{(1:3)}$ layer, $GelSP_{(1:4)}$ layer and bilayer scaffolds of $3DSP_{(1:3)}$/$GelSP_{(1:4)}$ with a 20 % deformation. Degradation ratio(h), Swelling rate(i), Porosity(j), Compressive modulus(k) and Young's modulus(l) of the of $SP_{(1:3)}$ layer, $GelSP_{(1:4)}$ layer and bilayer scaffolds of $3DSP_{(1:3)}$/$GelSP_{(1:4)}$.(ns, no significant difference; *$p < 0.05$. **$p < 0.01$).

fibrocartilage. However, the defects in the $3DSP_{(1:3)}$/$GelSP_{(1:4)}$ group were repaired with a limited cartilage-like tissues. At 12 weeks, the control group still presented unfilled defects. A smooth transition between repaired and natural tissue was observed in both $3DSP_{(1:3)}$/$GelSP_{(1:4)}$ and $2DSP_{(1:3)}$/$GelSP_{(1:4)}$ groups. However, a distinct boundary was still discernible in the defect site of the $2DSP_{(1:3)}$/$GelSP_{(1:4)}$ group, which became less pronounced in the 3D scaffolds.

The regenerative effect of cartilage was further assessed by immunohistochemical staining for COL-II (indicated by brown color) (Fig. 8). The control group exhibited no positive expression at the defect sites observed at both 6 and 12weeks after surgery. At 6 weeks, only weak COL-II expression was observed in the $2DSP_{(1:3)}$/$GelSP_{(1:4)}$ and $3DSP_{(1:3)}$/$GelSP_{(1:4)}$ groups. At 12 weeks, the $2DSP_{(1:3)}$/$GelSP_{(1:4)}$ group still displayed weak expression, while a significant increase in COL-II positive cartilage tissue was evident in the $3DSP_{(1:3)}$/$GelSP_{(1:4)}$ group, which showed the most intense COL-II staining.

Subsequently, micro-CT reconstruction was conducted to assess recovery efficacy of subchondral bone. Defects remained obvious in the control and $2DSP_{(1:3)}$/$GelSP_{(1:4)}$ groups (Fig. 7d). After 12 weeks, the results of trabecular number (Tb.N) in the $2DSP_{(1:3)}$/$GelSP_{(1:4)}$ group (3.1 ± 0.38/mm) were slightly higher than those in the control group (3.0 ± 0.46/mm) (Fig. 6g). However, no significant difference was observed in both Tb.N and trabecular separation/spacing (Tb.SP) of the control and $2DSP_{(1:3)}$/$GelSP_{(1:4)}$ groups (Fig. 6f-g, $P > 0.05$), likely due to the limited sample size. The BV/TV in the $3DSP_{(1:3)}$/$GelSP_{(1:4)}$ group (19.31 ± 2.2 %) was higher than that of the control and $2DSP_{(1:3)}$/$GelSP_{(1:4)}$ groups (12.41 ± 1.2 %, 14.25 ± 1.6 %) ($P < 0.01$). Similarly, the $3DSP_{(1:3)}$/$GelSP_{(1:4)}$ group demonstrates superior performance in quantitative calculations of trabecular number (Tb.N) (4.0 ± 0.29/mm) and Tb.SP (0.20 ± 0.02 mm) (Fig. 6f-g, $P < 0.01$).

Based on positive results of micro-CT analysis, the regenerative potential of the subchondral bone was assessed by HE staining and IHC staining of OCN. As shown in Fig.7-8, the defect areas within the different groups show different degrees of regeneration, while a greater number of new tissues (bone tissue) were observed in the $3DSP_{(1:3)}$/$GelSP_{(1:4)}$ group compared to both the control and $2DSP_{(1:3)}$/$GelSP_{(1:4)}$

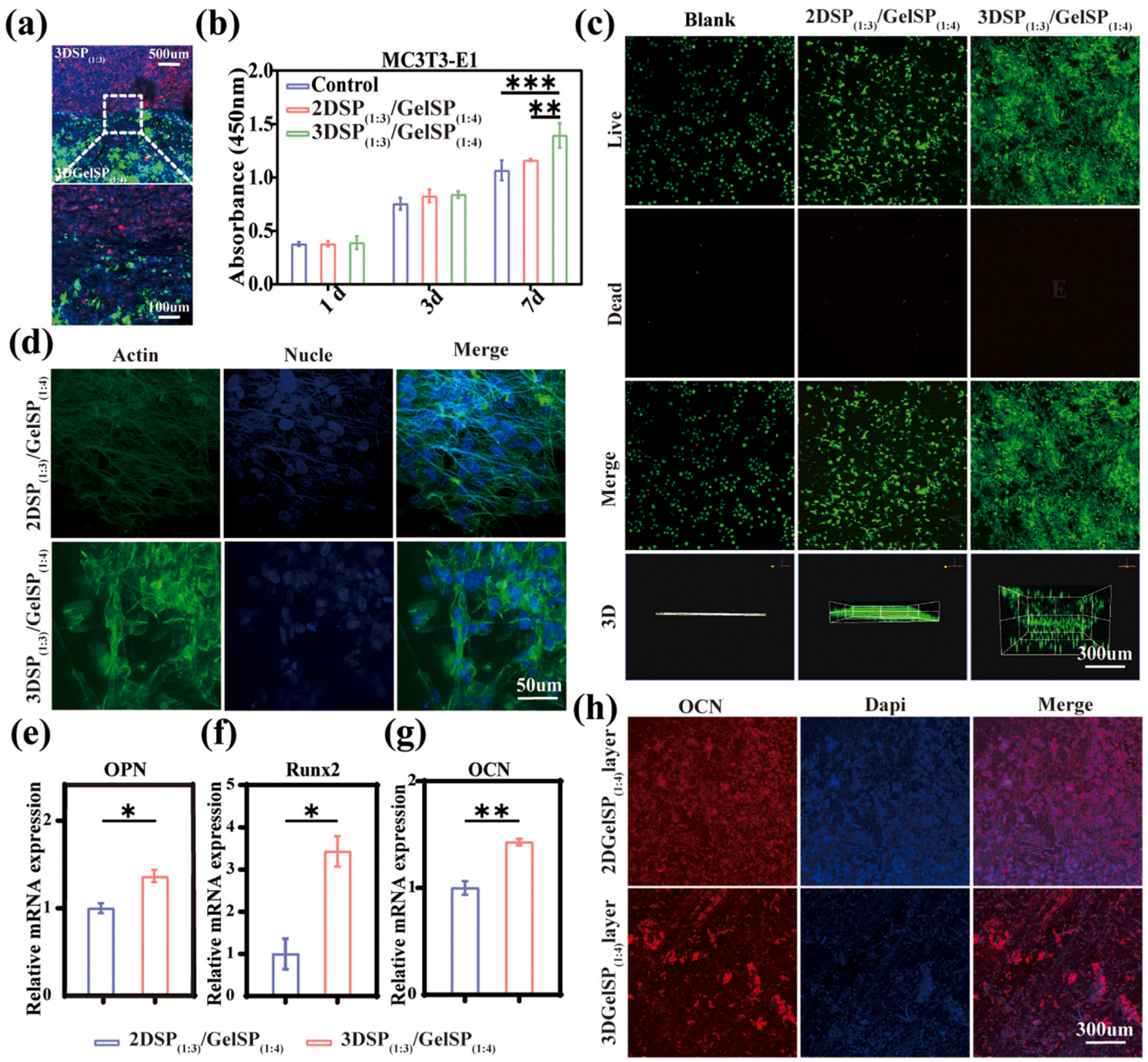

Fig. 4. Biocompatibility and osteogenic differentiation potential of MC3T3-E1 seeded on 2D/3D $SP_{(1:3)}/GelSP_{(1:4)}$ scaffolds. (a) The cell distribution inside $3DSP_{(1:3)}/GelSP_{(1:4)}$. Dil-labeled ATDC5(red) were seeded on the $SP_{(1:3)}$ layer, and Dio-labeled MC3T3-E1(green) were seeded on the $GelSP_{(1:4)}$ layer of $3DSP_{(1:3)}/GelSP_{(1:4)}$ for 7days. (b) Cell proliferation of MC3T3-E1 seeded on 2D/3D $SP_{(1:3)}/GelSP_{(1:4)}$ scaffolds at days 1, 3, and 7, as measured by the CCK-8 assay. (c) The viability of MC3T3-E1 seeded on 2D/3D $SP_{(1:3)}/GelSP_{(1:4)}$ scaffolds by live/dead staining and its 3D fluorescent images for 3 days. (d) Cytoskeleton staining of MC3T3-E1 cultured on different scaffolds for 3 days. (e–g) The relative mRNA expression levels of OPN, Runx2, and OCN of MC3T3-E1 seeded on 2D/3D $SP_{(1:3)}/GelSP_{(1:4)}$ scaffolds for 14 days. (h) Immunofluorescence images of osteocalcin (OCN) in MC3T3-E1 seeded on 2D/3D $SP_{(1:3)}/GelSP_{(1:4)}$ scaffolds. (*$p < 0.05$. **$p < 0.01$. ***$p < 0.001$).

groups (Fig. 7a and b). The defect area in the $3DSP_{(1:3)}/GelSP_{(1:4)}$ demonstrated the highest OCN deposition, which was consistent with the *in vitro* results. False positives were observed around the incompletely degraded scaffolds in both the $3DSP_{(1:3)}/GelSP_{(1:4)}$ and $2DSP_{(1:3)}/GelSP_{(1:4)}$ groups. Notably, new tissue replacement within the 3D scaffolds occurred at a faster rate than in the 2D membranes, with increased cell infiltration into the interior of the scaffold (Fig. 8).

4. Discussion

A persistent challenge in osteochondral defects repair lies on a stable integration between osteogenic and chondrogenic layers with natural interfaces. Previous studies have attempted to assembled bi- and multiphasic scaffolds through simple adhesion and freeze-drying processes [48]. However, these methods frequently led to delamination *in vivo*, separating newly formed cartilage from subchondral bone. This study introduced a well-designed method constructing integrated scaffolds for osteochondral defects. The scaffolds were developed through a one-step process that combined wet electrospinning with gas foaming technologies, resulting in a natural and stable interface between two layers. The 3D nanofibers scaffolds, which mimic the structure of native joint tissue and interface, provide ample internal space for cell proliferation and

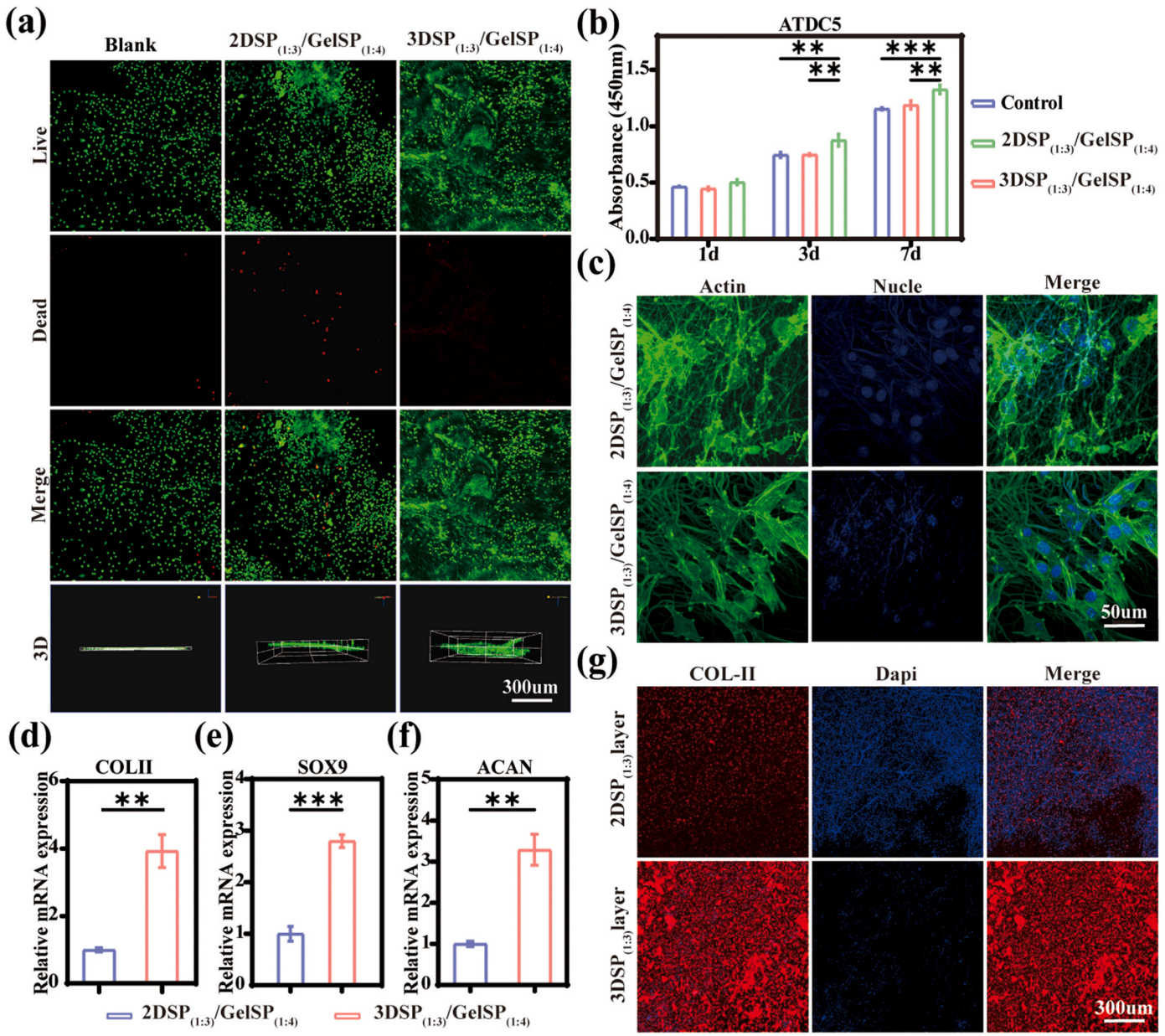

Fig. 5. Biocompatibility and chondrogenic differentiation potential of ATDC5 seeded on 2D/3D $SP_{(1:3)}$/$GelSP_{(1:4)}$ scaffolds. (a) The viability of ATDC5 seeded on 2D/3D $SP_{(1:3)}$/$GelSP_{(1:4)}$ scaffolds by live/dead staining and its 3D fluorescent images for 3 days. (b) Cell proliferation of ATDC5 seeded on 2D/3D $SP_{(1:3)}$/$GelSP_{(1:4)}$ scaffolds at days 1, 3, and 7, as measured by the CCK-8 assay. (c) Cytoskeleton staining of ATDC5 cultured on different scaffolds for 3 days. (d–f) The relative mRNA expression levels of COL-II, SOX-9 and ACAN of ATDC5 seeded on 2D/3D $SP_{(1:3)}$/$GelSP_{(1:4)}$ scaffolds for 14 days. (g) Immunofluorescence staining of COL-II in ATDC5 seeded on 2D/3D $SP_{(1:3)}$/$GelSP_{(1:4)}$ scaffolds for 14 days. (ns, no significant difference; *p < 0.05. **p < 0.01. ***p < 0.001).

spreading. In addition, the differences between mechanical properties and porous structures of two layers created a dual-differential micro-environment, effectively maintaining chondrogenic and osteogenic phenotypes of cells at the same time.

Electrospinning exhibited a substantial potential for scalable, precise production of nanofiber materials and has attracted significant attention in tissue engineering [49–51]. However, the dense packing fibers and limited thickness in traditional electrospun films restricted cellular infiltration [52,53]. Transitioning from 2D membranes to 3D scaffolds has broadened their applications. Numerous post-processing techniques, including short nanofiber assembly and 3D printing combined with electrospinning, allowed for controlled sizes and features, but the specialized and expensive equipment were required [54]. Some direct enhancement methods, such as wet-electrospinning, yield loosely structured scaffolds, but provided limited improvements in porosity [55]. Gas foaming technique offered a simple construction method to stretch 2D electrospun films into 3D scaffolds that preserved nano-topographical cues, which were essential for cell attachment and differentiation [56]. In addition, wet-electrospinning reduced fiber surface tension and provide convenience for gas foaming.

In this study, we combine the technologies of wet-electrospinning and gas foaming to construct the integrated scaffolds with varying ratios of SF/PCL. According to the results of the previous studies, the integrated scaffolds with similar components in different layers were more likely to facilitate a smooth interface transition [12,46]. In addition, the osteochondral scaffolds designed with internally graded composition, mechanical properties, and comparable swelling behavior have been shown to effectively prevent delamination [57–59].

SF and PCL were selected as the based materials due to their widespread applications in bone and cartilage tissue engineering [60–64].

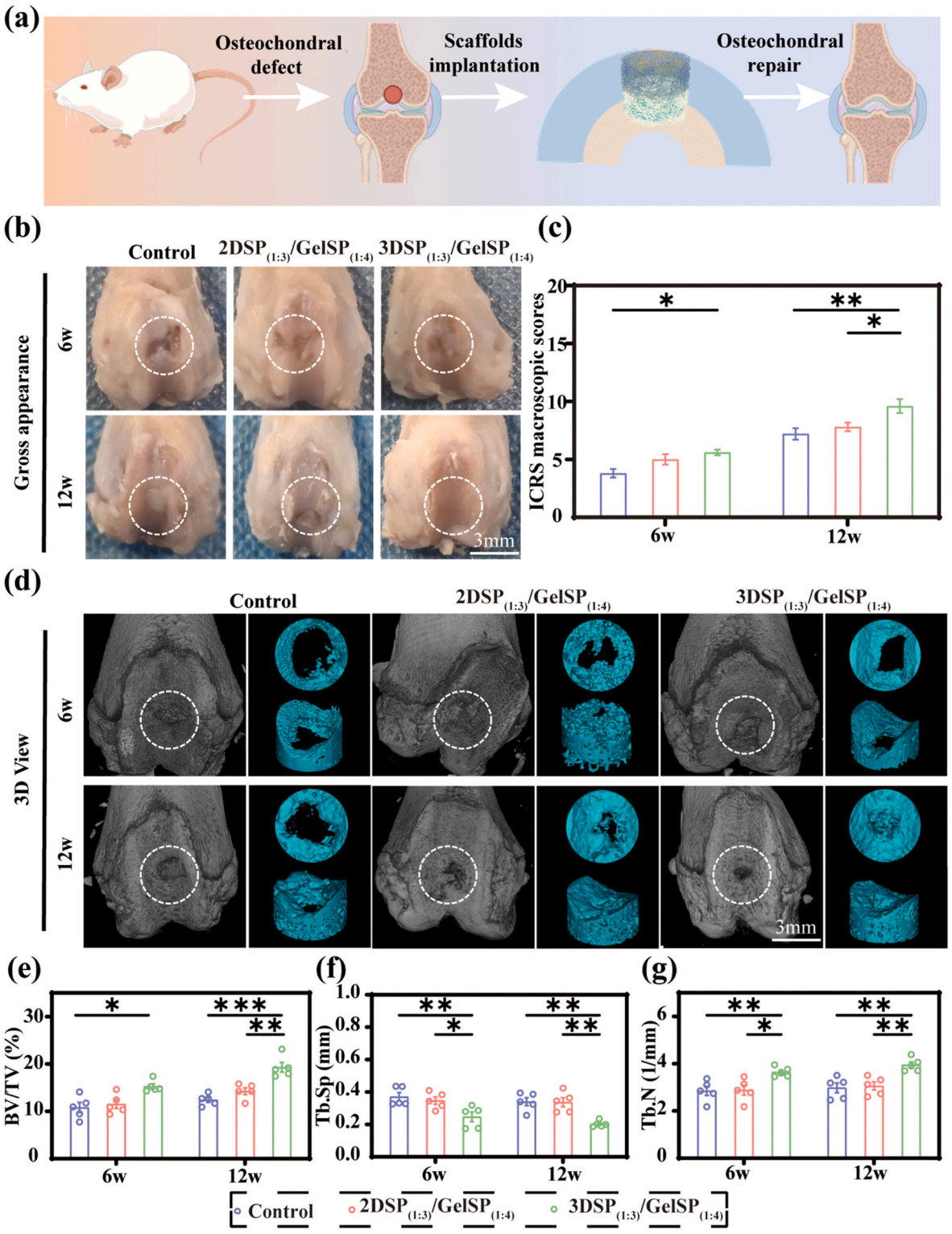

Fig. 6. Gross observation and radiological evaluation of the rat osteochondral defects. (a) Schematic diagram depicting process of the animal experiments, illustrated by Figure Draw. (b) Gross appearance. (c) ICRS macroscopic repair score. (d) The 3D reconstruction through micro-CT. (e–g) Quantitative analysis of bone volume proportion (BV/TV), trabecular separation/spacing (Tb.Sp), and trabecular number (Tb.N) within the subchondral bone of the defect area. (defects were presented in the white circles). (*$p < 0.05$. **$p < 0.01$. ***$p < 0.001$).

PCL, an FDA-approved implantable material, is known for its excellent mechanical properties and biodegradability. The incorporation of SF could enhance biocompatibility and cell adhesion properties of the PCL-based scaffolds, making them well-suited for osteochondral applications.

The primary objective in designing a scaffold for osteochondral repair is to maintain the phenotype of chondrocytes and osteoblasts, fostering a conducive microenvironment for tissue regeneration [65]. In this study, an integrated bilayer scaffold with dual-differential micro-environment was manufactured. The structural pore size of

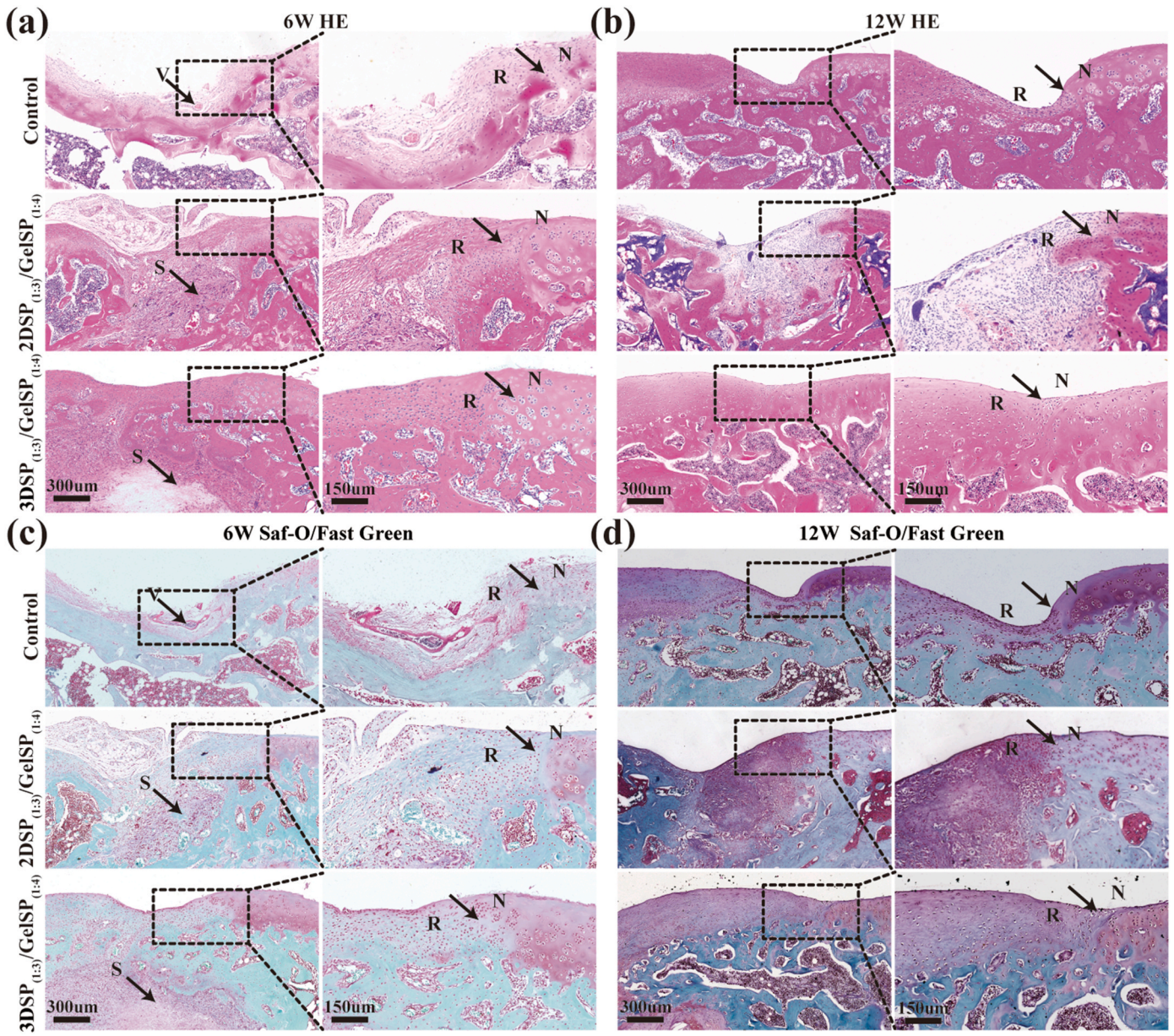

Fig. 7. Histological staining of the osteochondral defect *in vivo* at 6 and 12 weeks. Representative images of HE staining (a, b) and Safranin O/Fast Green staining (c, d) (The images on the right are magnified views of the left images, with black arrows indicating the boundary between normal cartilage (N) and repaired cartilage (R). V represents vessel, S represents incompletely degraded scaffolds). (For interpretation of the references to color in this figure legend, the reader is referred to the Web version of this article.)

osteochondral scaffolds is essential for inducting of osteogenic or chondrogenic differentiation [66]. Previous studies have demonstrated the optimal pore size for chondrogenic differentiation was 20–50 μm, while larger pores were conducive to mineralized tissue formation [67,68]. Therefore, it's crucial for optimal ratios of 1:3 and 1:4, as too small pole size would restrict infiltration of cells. A gelatin coating was introduced to bone layer of the porous scaffolds to enhance bone formation and elastic stress [31]. Experimental results demonstrated that the osteogenic layer exhibited enhanced mechanical strength compared to the uncoated state, while preserving natural interface integrity of bi-layer scaffolds. Indeed, gelatin-coated expanded 3D nanofiber scaffolds had been proven to exhibit super-elastic and shape-recovery properties without compromising their structural integrity [69]. In vitro results showed that 3D scaffolds effectively maintained the cellular phenotype, and the expression of genes such as OCN and Col-II were significantly enhanced. These findings indicated that the $3DSP_{(1:3)}/GelSP_{(1:4)}$ scaffolds closely mimicked dual different microenvironments in osteochondral tissue. Similar findings by Chen et al. demonstrated that the 3D scaffolds fabricated via gas foaming technology could enhance the expression of osteogenic specific genes [53,70].

A significant enhancement in the regeneration of osteochondral defects was observed in 3D scaffolds groups, which consisted with the *in vitro* results. The 3D scaffolds facilitated the exchange of nutrients and waste products while preserving nano-topographical cues essential for tissue healing and differentiation. High-porosity scaffolds have been shown to promote cellular infiltration, enhance wound healing, modulate the foreign body response and support extracellular matrix production [71,72]. Additionally, the increased surface-to-volume ratio of the 3D scaffolds accelerated degradation rate *in vivo*, thereby promoting tissue growth [73]. Moreover, the dual differentiation microenvironment in the 3D scaffolds provided guidance for homogenization and specific differentiation of stem cells [74]. In contrast, fibrous tissue

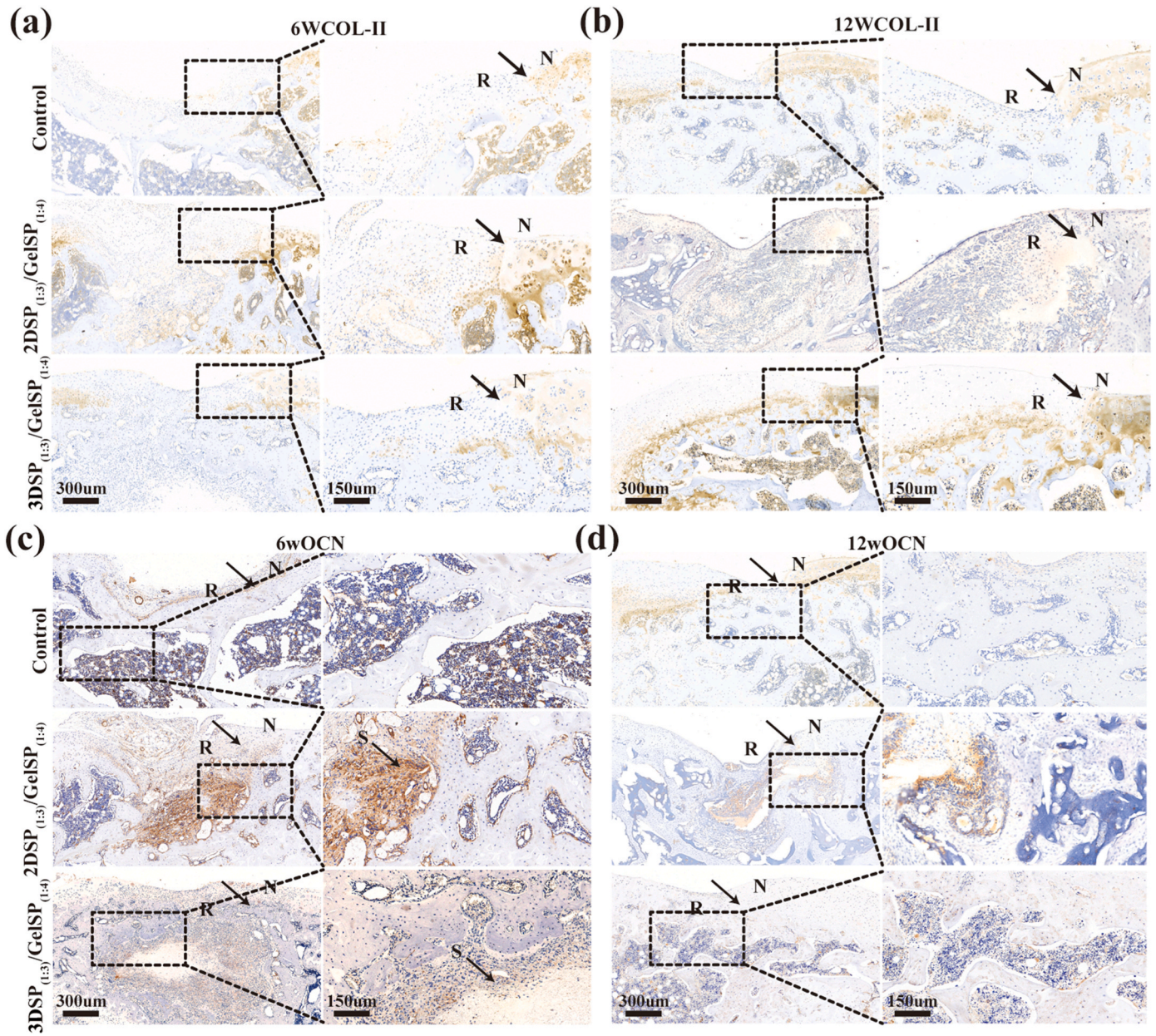

Fig. 8. Immunological assessment of osteochondral defect *in vivo* at 6 and 12 weeks. Representative images of COL-II (a, b) and OCN (c, d) immunohistochemical staining (The images on the right are magnified views of the left images, with black arrows indicating the boundary between normal cartilage (N) and repaired cartilage (R), V represents vessel, S represents incompletely degraded scaffolds).

repair was observed in the defects of the control group due to the lack of scaffold guidance and insufficient cellular sources. Partial subchondral bone regeneration was noted in the defects treated with 2D electrospun films. Although numerous studies have attempted to construct electrospun films for cartilage regeneration, most of them have focused on *in vitro* experiments due to inadequate mechanical support and hinder cellular infiltration [75,76]. In addition, engineered cartilage constructed from BMSC-loaded electrospun films frequently undergoes endochondral ossification after *in vivo* implantation, which further limits its applicability [77].

Although the *in vivo* experiments utilizing $3DSP_{(1:3)}/GelSP_{(1:4)}$ yielded promising results, further studies are required to elucidate the detailed mechanisms of osteogenic and chondrogenic differentiation. Moreover, integrating drug or growth factor release systems into the porous structure or coating may enhance mechanical properties and promote efficient tissue regeneration, representing a promising direction for future research [78].

5. Conclusion

In conclusion, a novel integrated scaffolds featuring heterogeneous bi-phasic structure ($3DSP_{(1:3)}/GelSP_{(1:4)}$) was successfully developed using a combination technique of layer-by-layer wet electrospinning, gas foaming, and asymmetric coating. Notably, the $3DSP_{(1:3)}/GelSP_{(1:4)}$ demonstrated favorable mechanical property properties and excellent biocompatibility. In addition, the 3D scaffolds not only closely mimicked the microenvironment of articular cartilage and subchondral bone than their 2D films, but also effectively maintained the chondroblast and osteoblast phenotypes. Furthermore, the 3D scaffolds enabled successful regeneration of subchondral bone and hyaline cartilage within 12 weeks. This study proposes a straightforward approach for constructing scaffolds that regulate cellular behavior, demonstrating

promising potential for applications in osteochondral tissue and interface repair.

CRediT authorship contribution statement

Zexing Zhang: Writing – original draft, Resources, Methodology, Investigation, Data curation, Conceptualization. **Qingquan Dong:** Visualization, Methodology, Investigation. **Zubing Li:** Writing – review & editing, Supervision, Funding acquisition, Conceptualization. **Gu Cheng:** Writing – review & editing, Supervision, Project administration, Funding acquisition, Conceptualization. **Zhi Li:** Writing – review & editing, Supervision, Project administration, Funding acquisition.

Declaration of competing interest

The authors declare that they have no known competing financial interests or personal relationships that could have appeared to influence the work reported in this paper.

Acknowledgments

This study was supported by grants from the National Natural Science Foundation of China (31870971 and 82170932); Basic Scientific Project of Wenzhou Medical University (KYYW202312); Knowledge Innovation Project of Wuhan (230171408).

Appendix. ASupplementary data

Supplementary data to this article can be found online at https://doi.org/10.1016/j.mtbio.2025.101737.

Data availability

Data will be made available on request.

References

[1] J.D. Steinmetz, G.T. Culbreth, L.M. Haile, Q. Rafferty, J. Lo, K.G. Fukutaki, J. A. Cruz, A.E. Smith, S.E. Vollset, P.M. Brooks, M. Cross, A.D. Woolf, H. Hagins, M. Abbasi-Kangevari, A. Abedi, I.N. Ackerman, H. Amu, B. Antony, J. Arabloo, A. Y. Aravkin, A.M. Argaw, A.A. Artamonov, T. Ashraf, A. Barrow, L.M. Bearne, I. M. Bensenor, A.Y. Berhie, N. Bhardwaj, P. Bhardwaj, V.S. Bhojaraja, A. Bijani, P. S. Briant, A.M. Briggs, N.S. Butt, J. Charan, V.K. Chattu, F.M. Cicuttini, K. Coberly, O. Dadras, X. Dai, L. Dandona, R. Dandona, K. de Luca, E. Denova-Gutiérrez, S. D. Dharmaratne, M. Dhimal, M. Dianatinasab, K.E. Dreinhoefer, M. Elhadi, U. Farooque, H.R. Farpour, I. Filip, F. Fischer, M. Freitas, B. Ganesan, B.N. B. Gemeda, T. Getachew, S.-H. Ghamari, A. Ghashghaee, T.K. Gill, M. Golechha, D. Golinelli, B. Gupta, V.B. Gupta, V.K. Gupta, R. Haddadi, N. Hafezi-Nejad, R. Halwani, S. Hamidi, A. Hanif, N.I. Harlianto, J.M. Haro, J. Hartvigsen, S.I. Hay, J.J. Hebert, G. Heidari, M.-S. Hosseini, M. Hosseinzadeh, A.K. Hsiao, I.M. Ilic, M. D. Ilic, L. Jacob, R. Jayawardena, R.P. Jha, J.B. Jonas, N. Joseph, H. Kandel, I. M. Karaye, M.J. Khan, Y.J. Kim, A.-A. Kolahi, O. Korzh, R. Koteeswaran, V. Krishnamoorthy, G.A. Kumar, N. Kumar, S. Lee, S.S. Lim, S.W. Lobo, G. Lucchetti, M.-R. Malekpour, A.A. Malik, L.G.G. Mandarano-Filho, S. Martini, A.-F.A. Mentis, M.K. Mesregah, T. Mestrovic, E.M. Mirrakhimov, A. Misganaw, R. Mohammadpourhodki, A.H. Mokdad, S. Momtazmanesh, S.D. Morrison, C.J. L. Murray, H. Nassereldine, H.B. Netsere, S. Neupane Kandel, M.O. Owolabi, S. Panda-Jonas, A. Pandey, S. Pawar, P. Pedersini, J. Pereira, A. Radfar, M.-M. Rashidi, D.L. Rawaf, S. Rawaf, R. Rawassizadeh, S.-M. Rayegani, D. Ribeiro, L. Roever, B. Saddik, A. Sahebkar, S. Salehi, L. Sanchez Riera, F. Sanmarchi, M. M. Santric-Milicevic, S. Shahabi, M.A. Shaikh, E. Shaker, M. Shannawaz, R. Sharma, S. Sharma, J.K. Shetty, R. Shiri, P. Shobeiri, D.A.S. Silva, A. Singh, J. A. Singh, S. Singh, S.T. Skou, H. Slater, M.S. Soltani-Zangbar, A.V. Starodubova, A. Tehrani-Banihashemi, S. Valadan Tahbaz, P.R. Valdez, B. Vo, L.G. Vu, Y.-P. Wang, S.H. Yahyazadeh Jabbari, N. Yonemoto, I. Yunusa, L.M. March, K.L. Ong, T. Vos, J.A. Kopec, Global, regional, and national burden of osteoarthritis, 1990–2020 and projections to 2050: a systematic analysis for the global burden of disease study 2021, Lancet Rheumatol 5 (2023) e508–e522, https://doi.org/10.1016/S2665-9913(23)00163-7.

[2] E.A. Makris, A.H. Gomoll, K.N. Malizos, J.C. Hu, K.A. Athanasiou, Repair and tissue engineering techniques for articular cartilage, Nat. Rev. Rheumatol. 11 (2015) 21–34, https://doi.org/10.1038/nrrheum.2014.157.

[3] M. Cucchiarini, H. Madry, Biomaterial-guided delivery of gene vectors for targeted articular cartilage repair, Nat. Rev. Rheumatol. 15 (2019) 18–29, https://doi.org/10.1038/s41584-018-0125-2.

[4] Z. Zhou, J. Cui, S. Wu, Z. Geng, J. Su, Silk fibroin-based biomaterials for cartilage/osteochondral repair, Theranostics 12 (2022) 5103–5124, https://doi.org/10.7150/thno.74548.

[5] G. Cheng, J. Dai, J. Dai, H. Wang, S. Chen, Y. liu, X. Liu, X. Li, X. Zhou, H. Deng, Z. Li, Extracellular matrix imitation utilizing nanofibers-embedded biomimetic scaffolds for facilitating cartilage regeneration, Chem. Eng. J. 410 (2021) 128379, https://doi.org/10.1016/j.cej.2020.128379.

[6] G. Yang, C. Qin, J. Chen, Z. Yang, W. Ma, Z. Cao, X. Zhao, L. Chen, C. Wu, Q. Yao, Black bioceramic scaffolds with micro/nano surface structure inducing mild hyperthermal environment for regenerating osteochondral defects, Nano Today 57 (2024) 102387, https://doi.org/10.1016/j.nantod.2024.102387.

[7] F. Yang, Y. Li, L. Wang, H. Che, X. Zhang, H. Jahr, L. Wang, D. Jiang, H. Huang, J. Wang, Full-thickness osteochondral defect repair using a biodegradable bilayered scaffold of porous zinc and chondroitin sulfate hydrogel, Bioact. Mater. 32 (2024) 400–414, https://doi.org/10.1016/j.bioactmat.2023.10.014.

[8] X. Meng, L. Li, C. Huang, K. Shi, Q. Zeng, C. Wen, S. Grad, M. Alini, L. Qin, X. Wang, Anti-inflammatory and anabolic biphasic scaffold facilitates osteochondral tissue regeneration in osteoarthritic joints, J. Mater. Sci. Technol. 156 (2023) 20–31, https://doi.org/10.1016/j.jmst.2023.01.035.

[9] C. Ai, Y.H.D. Lee, X.H. Tan, S.H.S. Tan, J.H.P. Hui, J.C.-H. Goh, Osteochondral tissue engineering: perspectives for clinical application and preclinical development, J. Orthop. Transl. 30 (2021) 93–102, https://doi.org/10.1016/j.jot.2021.07.008.

[10] L. Zhang, W. Dai, C. Gao, W. Wei, R. Huang, X. Zhang, Y. Yu, X. Yang, Q. Cai, Multileveled hierarchical hydrogel with continuous biophysical and biochemical gradients for enhanced repair of full-thickness osteochondral defect, Adv. Mater. 35 (2023) 2209565, https://doi.org/10.1002/adma.202209565.

[11] L. Zhou, J. Xu, A. Schwab, W. Tong, J. Xu, L. Zheng, Y. Li, Z. Li, S. Xu, Z. Chen, L. Zou, X. Zhao, G.J.V.M. van Osch, C. Wen, L. Qin, Engineered biochemical cues of regenerative biomaterials to enhance endogenous stem/progenitor cells (ESPCs)-mediated articular cartilage repair, Bioact. Mater. 26 (2023) 490–512, https://doi.org/10.1016/j.bioactmat.2023.03.008.

[12] L. Zhou, P. Guo, M. D'Este, W. Tong, J. Xu, H. Yao, M.J. Stoddart, G.J.V.M. van Osch, K.K.-W. Ho, Z. Li, L. Qin, Functionalized hydrogels for articular cartilage tissue engineering, Engineering 13 (2022) 71–90, https://doi.org/10.1016/j.eng.2022.03.008.

[13] L. Zhou, V.O. Gjvm, J. Malda, M.J. Stoddart, Y. Lai, R.G. Richards, K. Ki-wai Ho, L. Qin, Innovative tissue-engineered strategies for osteochondral defect repair and regeneration: current progress and challenges, Adv. Healthcare Mater. 9 (2020) 2001008, https://doi.org/10.1002/adhm.202001008.

[14] D. Lin, M. Li, L. Wang, J. Cheng, Y. Yang, H. Wang, J. Ye, Y. Liu, Multifunctional hydrogel based on silk fibroin promotes tissue repair and regeneration, Adv. Funct. Mater. 34 (2024) 2405255, https://doi.org/10.1002/adfm.202405255.

[15] Y. Lai, Y. Li, H. Cao, J. Long, X. Wang, L. Li, C. Li, Q. Jia, B. Teng, T. Tang, J. Peng, D. Eglin, M. Alini, D.W. Grijpma, G. Richards, L. Qin, Osteogenic magnesium incorporated into PLGA/TCP porous scaffold by 3D printing for repairing challenging bone defect, Biomaterials 197 (2019) 207–219, https://doi.org/10.1016/j.biomaterials.2019.01.013.

[16] C. Gao, W. Dai, X. Wang, L. Zhang, Y. Wang, Y. Huang, Z. Yuan, X. Zhang, Y. Yu, X. Yang, Q. Cai, Magnesium gradient-based hierarchical scaffold for dual-lineage regeneration of osteochondral defect, Adv. Funct. Mater. 33 (2023) 2304829, https://doi.org/10.1002/adfm.202304829.

[17] M. Hou, Y. Zhang, Y. Liu, X. Ge, X. Hu, Z. Zhao, X. Tian, T. Liu, H. Yang, X. Chen, F. He, X. Zhu, Biomimetic melatonin-loaded silk fibroin/GelMA scaffold strengthens cartilage repair through retrieval of mitochondrial functions, J. Mater. Sci. Technol. 146 (2023) 102–112, https://doi.org/10.1016/j.jmst.2022.10.031.

[18] Y. Cao, H. Zhang, M. Qiu, Y. Zheng, X. Shi, J. Yang, Biomimetic injectable and bilayered hydrogel scaffold based on collagen and chondroitin sulfate for the repair of osteochondral defects, Int. J. Biol. Macromol. 257 (2024) 128593, https://doi.org/10.1016/j.ijbiomac.2023.128593.

[19] H. Meng, X. Liu, R. Liu, Y. Zheng, A. Hou, S. Liu, W. He, Y. Wang, A. Wang, Q. Guo, J. Peng, Decellularized laser micro-patterned osteochondral implants exhibit zonal recellularization and self-fixing for osteochondral regeneration in a goat model, J. Orthop. Transl. 46 (2024) 18–32, https://doi.org/10.1016/j.jot.2024.04.005.

[20] X. Liu, Y. Chen, A.S. Mao, C. Xuan, Z. Wang, H. Gao, G. An, Y. Zhu, X. Shi, C. Mao, Molecular recognition-directed site-specific release of stem cell differentiation inducers for enhanced joint repair, Biomaterials 232 (2020) 119644, https://doi.org/10.1016/j.biomaterials.2019.119644.

[21] Y. Zhu, L. Kong, F. Farhadi, W. Xia, J. Chang, Y. He, H. Li, An injectable continuous stratified structurally and functionally biomimetic construct for enhancing osteochondral regeneration, Biomaterials 192 (2019) 149–158, https://doi.org/10.1016/j.biomaterials.2018.11.017.

[22] S. Barui, D. Ghosh, C.T. Laurencin, Osteochondral regenerative engineering: challenges, state-of-the-art and translational perspectives, Regen. Biomater. 10 (2022) rbac109, https://doi.org/10.1093/rb/rbac109.

[23] T. Yang, C. Ma, C. Lin, J. Wang, W. Qiao, L. Ling, Z. Yu, Y. Zhang, Innovative fabrication of ultrasensitive and durable graphene fiber aerogel for flexible pressure sensors, Carbon 229 (2024) 119484, https://doi.org/10.1016/j.carbon.2024.119484.

[24] M. Sadeghi-Ghadikolaei, E. Vasheghani-Farahani, F. Bagheri, A.K. Moghaddam, A. Mellati, A. Karimizade, Fabrication of 3D chitosan/polyvinyl alcohol/brushite nanofibrous scaffold for bone tissue engineering by electrospinning using a novel falling film collector, Int. J. Biol. Macromol. 272 (2024) 132874, https://doi.org/10.1016/j.ijbiomac.2024.132874.

[25] X. Jing, H. Li, H.-Y. Mi, Y.-J. Liu, Y.-M. Tan, Fabrication of fluffy shish-kebab structured nanofibers by electrospinning, CO2 escaping foaming and controlled

crystallization for biomimetic tissue engineering scaffolds, Chem. Eng. J. 372 (2019) 785–795, https://doi.org/10.1016/j.cej.2019.04.194.
[26] Y. Chen, X. Dong, M. Shafiq, G. Myles, N. Radacsi, **umei Mo, recent advancements on three-dimensional electrospun nanofiber scaffolds for tissue engineering, Adv. Fiber Mater. 4 (2022) 959–986, https://doi.org/10.1007/s42765-022-00170-7.
[27] C. Wang, Y. Su, J. Xie, Advances in electrospun nanofibers: versatile materials and diverse biomedical applications, Acc. Mater. Res. 5 (2024) 987–999, https://doi.org/10.1021/accountsmr.4c00145.
[28] Y. Chen, W. Xu, M. Shafiq, J. Tang, J. Hao, X. Xie, Z. Yuan, X. Xiao, Y. Liu, X. Mo, Three-dimensional porous gas-foamed electrospun nanofiber scaffold for cartilage regeneration, J. Colloid Interface Sci. 603 (2021) 94–109, https://doi.org/10.1016/j.jcis.2021.06.067.
[29] J. Jiang, S. Chen, H. Wang, M.A. Carlson, A.F. Gombart, J. Xie, CO2-expanded nanofiber scaffolds maintain activity of encapsulated bioactive materials and promote cellular infiltration and positive host response, Acta Biomater. 68 (2018) 237–248, https://doi.org/10.1016/j.actbio.2017.12.018.
[30] S. Chen, H. Wang, V.L. Mainardi, G. Talò, A. McCarthy, J.V. John, M.J. Teusink, L. Hong, J. Xie, Biomaterials with structural hierarchy and controlled 3D nanotopography guide endogenous bone regeneration, Sci. Adv. 7 (2021) eabg3089, https://doi.org/10.1126/sciadv.abg3089.
[31] S.M.S. Shahriar, N.S. Polavoram, S.M. Andrabi, Y. Su, D. Lee, H.Q. Tran, S. J. Schindler, J. Xie, Transforming layered 2D mats into multiphasic 3D nanofiber scaffolds with tailored gradient features for tissue regeneration, BMEMat 2 (2024) e12065, https://doi.org/10.1002/bmm2.12065.
[32] S. Chen, A. McCarthy, J.V. John, Y. Su, J. Xie, Converting 2D nanofiber membranes to 3D hierarchical assemblies with structural and compositional gradients regulates cell behavior, Adv. Mater. 32 (2020) 2003754, https://doi.org/10.1002/adma.202003754.
[33] L. Huang, T. Wu, J. Sun, X. Lin, Y. Peng, R. Zhang, Y. Gao, S. Xu, Y. Sun, Y. Zhou, B. Duan, Biocompatible chitin-based janus hydrogel membranes for periodontal repair, Acta Biomater. 190 (2024) 219–232, https://doi.org/10.1016/j.actbio.2024.10.038.
[34] L. Yan, X. Yang, Y. Zhang, Y. Wu, Z. Cheng, S.B. Darling, L. Shao, Porous Janus materials with unique asymmetries and functionality, Mater. Today 51 (2021) 626–647, https://doi.org/10.1016/j.mattod.2021.07.001.
[35] L.D. Quarles, D.A. Yohay, L.W. Lever, R. Caton, R.J. Wenstrup, Distinct proliferative and differentiated stages of murine MC3T3-E1 cells in culture: an in vitro model of osteoblast development, J. Bone Miner. Res. 7 (1992) 683–692, https://doi.org/10.1002/jbmr.5650070613.
[36] S. Li, H. Yang, X. Qu, Y. Qin, A. Liu, G. Bao, H. Huang, C. Sun, J. Dai, J. Tan, J. Shi, Y. Guan, W. Pan, X. Gu, B. Jia, P. Wen, X. Wang, Y. Zheng, Multiscale architecture design of 3D printed biodegradable Zn-based porous scaffolds for immunomodulatory osteogenesis, Nat. Commun. 15 (2024) 3131, https://doi.org/10.1038/s41467-024-47189-5.
[37] C. Shukunami, C. Shigeno, T. Atsumi, K. Ishizeki, F. Suzuki, Y. Hiraki, Chondrogenic differentiation of clonal mouse embryonic cell line ATDC5 in vitro: differentiation-dependent gene expression of parathyroid hormone (PTH)/PTH-related peptide receptor, JCB (J. Cell Biol.) 133 (1996) 457–468, https://doi.org/10.1083/jcb.133.2.457.
[38] Y.-H. Lai, Y.-H. Chen, A. Pal, S.-H. Chou, S.-J. Chang, E.-W. Huang, Z.-H. Lin, S.-Y. Chen, Regulation of cell differentiation via synergistic self-powered stimulation and degradation behavior of a biodegradable composite piezoelectric scaffold for cartilage tissue, Nano Energy 90 (2021) 106545, https://doi.org/10.1016/j.nanoen.2021.106545.
[39] H. Yin, G. Tian, J. Zheng, Y. Tang, R. Yu, Z. Yan, J. Wu, Z. Ding, C. Ning, X. Yuan, X. Sui, S. Liu, Q. Guo, W. Guo, Chondrocyte-derived apoptotic vesicles enhance stem cell biological function for the treatment of cartilage injury, Chem. Eng. J. 497 (2024) 154501, https://doi.org/10.1016/j.cej.2024.154501.
[40] Z. Cao, H. Wang, J. Chen, Y. Zhang, Q. Mo, P. Zhang, M. Wang, H. Liu, X. Bao, Y. Sun, W. Zhang, Q. Yao, Silk-based hydrogel incorporated with metal-organic framework nanozymes for enhanced osteochondral regeneration, Bioact. Mater. 20 (2023) 221–242, https://doi.org/10.1016/j.bioactmat.2022.05.025.
[41] L. Ghasemi-Mobarakeh, M.P. Prabhakaran, M. Morshed, M.-H. Nasr-Esfahani, S. Ramakrishna, Electrospun poly(ε-caprolactone)/gelatin nanofibrous scaffolds for nerve tissue engineering, Biomaterials 29 (2008) 4532–4539, https://doi.org/10.1016/j.biomaterials.2008.08.007.
[42] G. Cheng, J. Chen, Q. Wang, X. Yang, Y. Cheng, Z. Li, H. Tu, H. Deng, Z. Li, Promoting osteogenic differentiation in pre-osteoblasts and reducing tibial fracture healing time using functional nanofibers, Nano Res. 11 (2018) 3658–3677, https://doi.org/10.1007/s12274-017-1934-3.
[43] W. Kong, R. Li, X. Zhao, L. Ye, Construction of a highly oriented poly(lactic acid)-based block polymer foam and its self-reinforcing mechanism, ACS Sustainable Chem. Eng. 11 (2023) 1133–1145, https://doi.org/10.1021/acssuschemeng.2c06493.
[44] F. Wang, H. Liu, Y. Li, Y. Li, Q. Ma, J. Zhang, X. Hu, Tunable biodegradable polylactide–silk fibroin scaffolds fabricated by a solvent-free pressure-controllable foaming technology, ACS Appl. Bio Mater. 3 (2020) 8795–8807, https://doi.org/10.1021/acsabm.0c01157.
[45] H. Wu, X. Wang, G. Wang, G. Yuan, W. Jia, L. Tian, Y. Zheng, W. Ding, J. Pei, Advancing scaffold-assisted modality for in situ osteochondral regeneration: a shift from biodegradable to bioadaptable, Adv. Mater. 36 (2024) 2407040, https://doi.org/10.1002/adma.202407040.
[46] D. Liu, X. Wang, C. Gao, Z. Zhang, Q. Wang, Y. Pei, H. Wang, Y. Tang, K. Li, Y. Yu, Q. Cai, X. Zhang, Biodegradable piezoelectric-conductive integrated hydrogel scaffold for repair of osteochondral defects, Adv. Mater. 36 (2024) 2409400, https://doi.org/10.1002/adma.202409400.
[47] Z. Xiong, F. Hong, Z. Wu, Y. Ren, N. Sun, B.C. Heng, J. Zhou, Gradient scaffolds for osteochondral tissue engineering and regeneration, Chem. Eng. J. 498 (2024) 154797, https://doi.org/10.1016/j.cej.2024.154797.
[48] W. Jiang, X. Xiang, M. Song, J. Shen, Z. Shi, W. Huang, H. Liu, An all-silk-derived bilayer hydrogel for osteochondral tissue engineering, Materials Today Bio 17 (2022) 100485, https://doi.org/10.1016/j.mtbio.2022.100485.
[49] L. Xiao, H. Liu, H. Huang, S. Wu, L. Xue, Z. Geng, L. Cai, F. Yan, 3D nanofiber scaffolds from 2D electrospun membranes boost cell penetration and positive host response for regenerative medicine, J. Nanobiotechnol. 22 (2024) 322, https://doi.org/10.1186/s12951-024-02578-2.
[50] M. Zhang, S. Xu, R. Wang, Y. Che, C. Han, W. Feng, C. Wang, W. Zhao, Electrospun nanofiber/hydrogel composite materials and their tissue engineering applications, J. Mater. Sci. Technol. 162 (2023) 157–178, https://doi.org/10.1016/j.jmst.2023.04.015.
[51] M. Kamaraj, N. Moghimi, J. Chen, R. Morales, S. Chen, A. Khademhosseini, J. V. John, New dimensions of electrospun nanofiber material designs for biotechnological uses, Trends Biotechnol. 42 (2024) 631–647, https://doi.org/10.1016/j.tibtech.2023.11.008.
[52] D. Zong, X. Zhang, X. Yin, F. Wang, J. Yu, S. Zhang, B. Ding, Electrospun fibrous sponges: principle, fabrication, and applications, Adv. Fiber Mater. 4 (2022) 1434–1462, https://doi.org/10.1007/s42765-022-00202-2.
[53] L. Xiao, H. Liu, S. Wu, H. Huang, Y. Xie, R. Wei, J. Lei, Y. Lei, L. Xue, F. Yan, Z. Geng, L. Cai, Fishnet-inspired 3D scaffold fabricated from mesh-like electrospun membranes promoted osteoporotic bone regeneration, Adv. Fiber Mater. (2024), https://doi.org/10.1007/s42765-024-00451-3.
[54] H. Zhu, J. Wang, S. Wang, Y. Yang, M. Chen, Q. Luan, X. Liu, Z. Lin, J. Hu, K. Man, J. Zhang, Additively manufactured bioceramic scaffolds based on triply periodic minimal surfaces for bone regeneration, J. Tissue Eng. 15 (2024) 20417314241244997, https://doi.org/10.1177/20417314241244997.
[55] J. Zhang, X. Zha, G. Liu, H. Zhao, X. Liu, L. Zha, Injectable extracellular matrix-mimetic hydrogel based on electrospun Janus fibers, Mater. Horiz. 11 (2024) 1944–1956, https://doi.org/10.1039/D3MH01789C.
[56] Y. Chen, W. Xu, Z. Pan, B. Li, X. Mo, Y. Li, J. Wang, Y. Wang, Z. Wei, Y. Chen, Z. Han, C. Lin, Y. Liu, X. Ye, J. Yu, Three-dimensional gas-foamed scaffolds decorated with metal phenolic networks for cartilage regeneration, Materials Today Bio 29 (2024) 101249, https://doi.org/10.1016/j.mtbio.2024.101249.
[57] W. Wei, W. Liu, H. Kang, X. Zhang, R. Yu, J. Liu, K. Huang, Y. Zhang, M. Xie, Y. Hu, H. Dai, A one-stone-two-birds strategy for osteochondral regeneration based on a 3D printable biomimetic scaffold with kartogenin biochemical stimuli gradient, Adv Healthcare Materials 12 (2023) 2300108, https://doi.org/10.1002/adhm.202300108.
[58] A. Schwab, M.A. Wesdorp, J. Xu, F. Abinzano, C. Loebel, M. Falandt, R. Levato, D. Eglin, R. Narcisi, M.J. Stoddart, J. Malda, J.A. Burdick, M. D'Este, G.J.V.M. van Osch, Modulating design parameters to drive cell invasion into hydrogels for osteochondral tissue formation, Journal of Orthopaedic Translation 41 (2023) 42–53, https://doi.org/10.1016/j.jot.2023.07.001.
[59] R. Sun, Q. Zhang, C. Yu, Y. Zhu, Y. Zheng, T. Gu, L. Ye, W. Yang, X. Ying, Y. Xu, S. Fan, R. Tang, W. Qi, S. Yao, Continuous-gradient mineralized hydrogel synthesized via gravitational osmosis for osteochondral defect repair, Adv. Funct. Mater. 34 (2024) 2408249, https://doi.org/10.1002/adfm.202408249.
[60] Y. Li, M. Chen, W. Zhou, S. Gao, X. Luo, L. Peng, J. Yan, P. Wang, Q. Li, Y. Zheng, S. Liu, Y. Cheng, Q. Guo, Cell-free 3D wet-electrospun PCL/silk fibroin/Sr2+ scaffold promotes successful total meniscus regeneration in a rabbit model, Acta Biomater. 113 (2020) 196–209, https://doi.org/10.1016/j.actbio.2020.06.017.
[61] X. Xing, G. Cheng, C. Yin, X. Cheng, Y. Cheng, Y. Ni, X. Zhou, H. Deng, Z. Li, Magnesium-containing silk fibroin/polycaprolactone electrospun nanofibrous scaffolds for accelerating bone regeneration, Arab. J. Chem. 13 (2020) 5526–5538, https://doi.org/10.1016/j.arabjc.2020.03.031.
[62] X. Wang, Y. Peng, Y. Wu, S. Cao, H. Deng, Z. Cao, Chitosan/silk fibroin composite bilayer PCL nanofibrous mats for bone regeneration with enhanced antibacterial properties and improved osteogenic potential, Int. J. Biol. Macromol. 230 (2023) 123265, https://doi.org/10.1016/j.ijbiomac.2023.123265.
[63] X. Xie, Y. Chen, X. Wang, X. Xu, Y. Shen, A. ur R. Khan, A. Aldalbahi, A.E. Fetz, G. L. Bowlin, M. El-Newehy, X. Mo, Electrospinning nanofiber scaffolds for soft and hard tissue regeneration, J. Mater. Sci. Technol. 59 (2020) 243–261, https://doi.org/10.1016/j.jmst.2020.04.037.
[64] X. Jia, J. Zhou, J. Ning, M. Li, Y. Yao, X. Wang, Y. Jian, K. Zhao, The polycaprolactone/silk fibroin/carbonate hydroxyapatite electrospun scaffold promotes bone reconstruction by regulating the polarization of macrophages, Regen. Biomater. 9 (2022) rbac035, https://doi.org/10.1093/rb/rbac035.
[65] D. Lin, B. Cai, L. Wang, L. Cai, Z. Wang, J. Xie, Q. Lv, Y. Yuan, C. Liu, S.G. Shen, A viscoelastic PEGylated poly(glycerol sebacate)-based bilayer scaffold for cartilage regeneration in full-thickness osteochondral defect, Biomaterials 253 (2020) 120095, https://doi.org/10.1016/j.biomaterials.2020.120095.
[66] Y. Sun, Y. You, W. Jiang, B. Wang, Q. Wu, K. Dai, 3D bioprinting dual-factor releasing and gradient-structured constructs ready to implant for anisotropic cartilage regeneration, Sci. Adv. 6 (2020) eaay1422, https://doi.org/10.1126/sciadv.aay1422.
[67] M. Sukul, P. Sahariah, H.L. Lauzon, J. Borges, M. Másson, J.F. Mano, H.J. Haugen, J.E. Reseland, In vitro biological response of human osteoblasts in 3D chitosan sponges with controlled degree of deacetylation and molecular weight, Carbohydr. Polym. 254 (2021) 117434, https://doi.org/10.1016/j.carbpol.2020.117434.

[68] J. Gao, X. Yu, X. Wang, Y. He, J. Ding, Biomaterial–Related cell microenvironment in tissue engineering and regenerative medicine, Engineering 13 (2022) 31–45, https://doi.org/10.1016/j.eng.2021.11.025.
[69] S. Chen, H. Wang, A. McCarthy, Z. Yan, H.J. Kim, M.A. Carlson, Y. Xia, J. Xie, Three-Dimensional objects consisting of hierarchically assembled nanofibers with controlled alignments for regenerative medicine, Nano Lett. 19 (2019) 2059–2065, https://doi.org/10.1021/acs.nanolett.9b00217.
[70] Y. Chen, Y. Li, X. Wang, X. Mo, Y. Chen, Z. Deng, X. Ye, J. Yu, One-step gas foaming strategy for constructing strontium nanoparticle decorated 3D scaffolds: a new platform for repairing critical bone defects, ACS Appl. Mater. Interfaces (2024), https://doi.org/10.1021/acsami.4c13119.
[71] Y. Chen, Z. Jia, M. Shafiq, X. Xie, X. Xiao, R. Castro, J. Rodrigues, J. Wu, G. Zhou, X. Mo, Gas foaming of electrospun poly(L-lactide-co-caprolactone)/silk fibroin nanofiber scaffolds to promote cellular infiltration and tissue regeneration, Colloids Surf. B Biointerfaces 201 (2021) 111637, https://doi.org/10.1016/j.colsurfb.2021.111637.
[72] S.M.S. Shahriar, A.D. McCarthy, S.M. Andrabi, Y. Su, N.S. Polavoram, J.V. John, M. P. Matis, W. Zhu, J. Xie, Mechanically resilient hybrid aerogels containing fibers of dual-scale sizes and knotty networks for tissue regeneration, Nat. Commun. 15 (2024) 1080, https://doi.org/10.1038/s41467-024-45458-x.
[73] D. Xu, Z. Li, Z. Deng, X. Nie, Y. Pan, G. Cheng, Degradation profiles of the poly (ε-caprolactone)/silk fibroin electrospinning membranes and their potential applications in tissue engineering, Int. J. Biol. Macromol. 266 (2024) 131124, https://doi.org/10.1016/j.ijbiomac.2024.131124.
[74] T. Wang, W. Xu, X. Zhao, B. Bai, Y. Hua, J. Tang, F. Chen, Y. Liu, Y. Wang, G. Zhou, Y. Cao, Repair of osteochondral defects mediated by double-layer scaffolds with natural osteochondral-biomimetic microenvironment and interface, Materials Today Bio 14 (2022) 100234, https://doi.org/10.1016/j.mtbio.2022.100234.
[75] Y. Chen, M. Shafiq, M. Liu, Y. Morsi, X. Mo, Advanced fabrication for electrospun three-dimensional nanofiber aerogels and scaffolds, Bioact. Mater. 5 (2020) 963–979, https://doi.org/10.1016/j.bioactmat.2020.06.023.
[76] A. Arash, F. Dehgan, S.Z. Benisi, M. Jafari-Nodoushan, M. Pezeshki-Modaress, Polysaccharide base electrospun nanofibrous scaffolds for cartilage tissue engineering: challenges and opportunities, Int. J. Biol. Macromol. 277 (2024) 134054, https://doi.org/10.1016/j.ijbiomac.2024.134054.
[77] T.-J. Ji, B. Feng, J. Shen, M. Zhang, Y.-Q. Hu, A.-X. Jiang, D.-Q. Zhu, Y.-W. Chen, W. Ji, Z. Zhang, H. Zhang, F. Li, An avascular niche created by axitinib-loaded PCL/collagen nanofibrous membrane stabilized subcutaneous chondrogenesis of mesenchymal stromal cells, Adv. Sci. 8 (2021) 2100351, https://doi.org/10.1002/advs.202100351.
[78] Y. Su, M.S. Toftdal, A. Le Friec, M. Dong, X. Han, M. Chen, 3D electrospun synthetic extracellular matrix for tissue regeneration, Small Science 1 (2021) 2100003, https://doi.org/10.1002/smsc.202100003.